UNIVERSITÀ
DEGLI STUDI
DI PADOVA

Sede Amministrativa: Università degli Studi di Padova

Dipartimento di Geoscienze

SCUOLA DI DOTTORATO DI RICERCA IN : SCIENZE DELLA TERRA
INDIRIZZO: UNICO
CICLO: 26

Pore-scale modelling of electrical phenomena in porous media with implications for induced polarization and self-potential methods

Direttore della Scuola : Ch.mo Prof. Massimiliano Zattin
Coordinatore d'indirizzo: Ch.mo Prof. Massimiliano Zattin
Supervisore :Ch.mo Prof. Giorgio Cassiani

Dottorando : Jose Bernardo Colmenares

Contents

List of Figures

Abstract

In this dissertation theoretical and numerical models are proposed for the induced polarization (IP) phenomenon. The theoretical model takes into account the contribution of Stern layer and membrane polarization in variably saturated sandy soils, while the numerical model can be used to get insight into the origins of the membrane polarization mechanism. In this dissertation the frequency-dependent bulk electrical conductivity of the porous medium is calculated using the Hashin-Shtrickman Average model, which describes the dielectric response of variably saturated porous media. Both stern and membrane polarization can be calculated independently, which allows us to study the effect of different physical parameters to each one. The results show that membrane polarization can be obscured by the Maxwell-Wagner polarization. The model was tested against data from laboratory measurements of sands with variable saturation and a good fit was obtained even though more work has to be done for low saturation levels. Then a numerical model is presented which uses the linearized Poisson-Boltzmann Equation to compute the electrostatic potential of an object in the presence of free ions. The solution is then used to calculate a the dielectric to be used on a numerical solver of Poisson's equation to calculate the impedance of the system. This result corroborates the assumptions behind the Short Narrow Pore model, a simplified and yet effective model describing membrane polarization. The methodology used requires a much lower computational effort than solving the Poisson-Nerst-Planck equation since there are no coupled systems.

Esposizione riassuntiva

In questa tesi sono proposti modelli teorici e numerici per il fenomeno di polarizzazione indotta (IP) . Il modello teorico prende in considerazione il contributo della polarizzazione dello strato di Stern e di membrana in terreni sabbiosi di saturazione variabile, mentre il modello numerico può essere utilizzato per ottenere una migliore comprensione degli origini dal meccanismo della polarizzazione di membrana. La conducibilità elettrica del mezzo poroso dipendente dalla frequenza viene calcolata utilizzando il modello Hashin - Shtrickman, che descrive la risposta dielettrica di mezzi porosi con saturazione variabile. Sia la polarizzazione di Stern e di membrana possono essere calcolati indipendentemente, cosa che ci permette studiare l'effetto di diverse parametri fisici. I risultati mostrano che la polarizzazione di membrana può essere oscurato dalla polarizzazione Maxwell - Wagner. Il modello è stato testato contro dati da misure di laboratorio di sabbia con saturazione variabile con buoni risultati anche se più lavoro deve essere fatto per i livelli di bassa saturazione. Il modello numerico presentato utilizza la equazione linearizzata di Poisson - Boltzmann per calcolare il potenziale elettrostatico di un oggetto in presenza di ioni liberi in soluzione. La soluzione viene quindi utilizzato per calcolare il dielettrico ad essere utilizzato su un risolutore numerico dell'equazione di Poisson per calcolare l'impedenza del sistema. Questo risultato avvalora le ipotesi alla base del modello short narrow pore, un modello semplificato ma efficace che descrive la polarizzazione di membrana. La metodologia utilizzata richiede uno sforzo computazionale molto inferiore che risolvere l'equazione di Poisson-Nerst-Planck poiché non esistono sistemi accoppiati.

Acknowledgements

This work was supported by the EU FP7 collaborative project iSOIL "Interactions between soil related sciences – Linking geophysics, soil science and digital soil mapping", the NIGMS, NIH, Grant no. 1R01GM093937-01 and the Italian Ministry of Education and Research through the Flagship (PB05) InterOmics. The authors also gratefully acknowledge the IIT platform Computation.

I would like to thank my advisor Giorgio Cassiani for his support, my team leader at the Italian Institute of Technology Walter Rocchia for all his advice, Alessandro Brovelli for his comments and corrections, my parents for teaching me the love for science, and to my wife Gabriella: Without her love and patience I would not have made it.

Chapter 1

Introduction

Most current process-based models for IP include consider either membrane polarization (e.g. Marshall and Madden, 1959, de Lima and Sharma, 1992, Titov et al., 2002, and refs therein) or grain polarization (e.g. Fixman, 1980, Dias, 2000, Revil's works), but not both.

Previous works (in particular, works from A. Revil, but also for example Klein and Sill, 1982) have shown that the characteristic relaxation time is correlated with the average grain diameter. This suggests that grain polarization is one of the major contributing mechanisms, in particular in sands/sandstones.

Recent experimental works highlighted the importance of pore space characteristics. In particular (1) [19] and [1] observed that the relaxation time is associated to the size of pore-throats in sandstones, (2) Kruschwitz [37] observed a clear correlation between texture, pore-space characteristics, pore-throat diameter and the relaxation time, and (3) Koch et al., 2011, found a shift in relaxation time with compaction of unconsolidated sediments, an observation which is difficult to explain considering grain polarization only. See also [18] for more literature on this and further insights. Moreover, theoretical and experimental work on micro/nanofluidic devices have shown that membrane polarization really occurs, although in this field it's called 'concentration polarization': see for example [24].

The aim of this dissertation is to develop a mechanistic model for induced polarization in the frequency domain that incorporates both grain and membrane polarization and uses a non-linear mixing rule to combine the (complex) contribution of the three phases (water, air and solid grains).

After the presentation of the theoretical model will be presented a numerical model to calculate the impedance of complex geometries with ionic solution. In particular, is well suited to study the membrane polarization mechanism. Madden [12] offered a theoretical model based on the serial connection of ion-selective and nonselective pores, which generate a difference in the cation and anion transport. Titov [43] proposed a model based on the existence of ion-selective narrow passages (called the Short Narrow Pores model, or SNP). This model describes the membrane polarization at different frequencies based on the assumption that the narrow passages are much shorter than the large ones, hence it is a special case of the Marshall-Madden model. This class of models are capable of describing many of the observed phenomena, using empirically derived parameters. However, these (and other) models suffer from an over-

simplification of the geometry and assume that the narrow or active pores exist, without any further explanation about their size or properties.

In this paper we aim at investigating the basic assumptions of these simplified models using an innovative, accurate computational approach. Numerical solutions of the Poisson-Boltzmann Equation (PBE) have been successfully applied particularly in biophysics thanks to the development of robust algorithms that can calculate the electrostatic potential of complex structures such as proteins and their associated electrostatic energy. We propose the use of the PBE to study the induced polarization phenomena. In particular, we aim at using the PBE to gain insight about the chargeability of a water-wet system composed of pores and pore throats, where membrane polarization plays a key role.

Volkmann [18] developed a numerical model using the Poisson-Nerst-Planck (PNP) coupled system using the finite element method. The PNP equations were transformed in the frequency domain, and no fixed charges on the surface were included in the model. In it, the region close to the mineral surface (and up to a Deby length from it) is assumed to have a lower anion mobility. The method was tested against the Titov's model with good results. Note that solving the PNP coupled system in the frequency domain for complex geometries can be a very expensive task from the computational point of view. For each frequency, solvers of the Poisson and Nerst-Planck equations are used until no difference between their solutions are found (under a certain threshold). This is due to the dependence of the electrostatic potential on the ion distribution (Poisson's equation) and the ion flow and distribution on the electrostatic potential (Nerst-Planck). In this work the Poisson-Boltzmann equation is used to calculate the electrostatic potential due to the charges on the surface of the mineral and ions in the pore space under a constant electric field. Under the assumption that the field is low when compared to the effect of the fixed charges in the mineral's surface, the solution of the Poisson-Boltzmann equation is used to calculate the conductivity in the pore's water. Then, Poisson's equation is used to calculate the impedance of the system threating the ion flow in the liquid phase as current in a semiconductor with variable conductivity.

Chapter 2

Theoretical modelling

2.1 Model description

The complex bulk electrical conductivity σ_b^* of a porous medium (or its reciprocal, the electrical resistivity) is a frequency dependent property,

$$\sigma_b^* = \frac{1}{\rho_b^*} = i\omega\epsilon^* \tag{2.1}$$

that can alternatively be expressed by the magnitude and phase angle, or by the in-phase and quadrature components,

$$\sigma^* = \|\sigma\| \exp(i\varphi) = \sigma' + i\sigma'' \tag{2.2}$$

$$\|\sigma\| = \sqrt{\sigma'^2 + \sigma''^2} \tag{2.3}$$

$$\tan(\varphi) = \sigma''/\sigma' \tag{2.4}$$

where the superscript * indicates a complex quantity. The frequency dependent behavior of electrical conductivity is associated to a number of polarization mechanisms that occur within the pores and around the solid grains. Specifically it is believed that three are the major mechanisms,

1. Maxwell-Wagner (MW) polarization. Polarization of the water-solid grain interface due to the accumulation of charges that occurs at relatively high frequencies ($\omega > 10 - 100Hz$). This type of polarization has been already extensively studied, and a number of mechanistic model exist, as for example [8].

2. Membrane polarization. The complex inner structure of the porous medium, formed by large pore-bodies and narrow pore-throats, combined with the EDL at the surface/water interface is responsible for the local accumulation of ions and the formation of a membrane potential. More specifically, the pore-throats with its have a negatively charged inner surface act as ion-selective channels. As a result, the concentration of ions at opposite boundaries of each pore-throat fluctuates (with opposite sign) and each pore behaves like an electrical capacitor. Until recently, this has been considered the primary polarization mechanism, and included in a number of models [13, 25, 26, 43, 44].

3. Electrical double layer (EDL) polarization. This polarization mechanism has been considered only in the recent years, and models based on this mechanism proved able to identify textural and hydraulic properties of porous material [4, 23, 29–31]. These models are mostly based on the theories of [38, 39] for EDL polarization around a spherical particle. For the good predictive capabilities of the models based upon this electrochemical polarization mechanism, it is gaining increasing attention. Despite this, understanding of EDL polarization (and the interplay between polarization mechanisms and the inner structure of the porous medium) is still in its infancy. In particular, it is unclear whether both the Stern (inner) and diffuse layers polarize (as suggested for example by De Lima and Sharma, 1992). Leroy and Revil, 2009a; Leroy and Revil, 2009b; Revil and Florsch, 2010, postulated instead that only the Stern layer contributes to polarization, as it is disconnected at the scale of the grains (in other words, the Stern layer of each grain does not overlap with that of the adjacent grains). The diffuse layer instead forms a continuous structure, and therefore electrochemical gradients cannot build-up.

EDL and membrane polarization are the more likely mechanisms responsible for the low ($0 \leq \omega \geq 10Hz$) frequency variations of the electrical conductivity of granular porous media (Leroy and Revil, 2009a). The specific objective of this work was to develop a mechanistic model suitable to understand and predict the frequency dependent behavior of granular porous materials (soils and sedimentary geological formations) in the low frequency range. The model developed in this work has at least three strengths, (i) it includes both EDL and membrane polarization, and (ii) it is process-based, and all parameters have a clear physical meaning and (iii) it uses a non-linear mixing equation to combine the complex conductivity of each phase (solid, water and non-aqueous). Since MW polarization has been extensively studied in other works, and experimental data above 100Hz, the frequency range where MW polarization becomes dominant, are often affected by artifacts and instrumentation noise, its contribution was not considered.

2.1.1 Stern layer polarization

Following (Leroy and Revil, 2009a; Revil and Florsch, 2010), it was assumed that only the Stern layer of the EDL can polarize, that is, the diffuse layer conductivity is not frequency-dependent. The total complex surface conductivity was modeled using the approach of (De Lima and Sharma, 1992), later adopted also by (Leroy and Revil, 2009a; Revil and Florsch, 2010; Schmutz et al., 2010)

$$\sigma_s^* = \frac{4}{d_0}\left[\Sigma^d + \Sigma^s\left(1 - \frac{1}{1 + i\omega\tau_0}\right)\right] \tag{2.5}$$

According to this model, in the direct current (DC) limit, the surface conductivity is simply due to the excess of charge in the diffuse layer, while the contribution of the Stern layer is negligible,

$$\sigma_s^* = \frac{4}{d_0}\Sigma^d \tag{2.6}$$

On the contrary, at high frequencies (in the static limit) both the Stern and diffuse layer contribute to surface conductivity,

$$\sigma_s^* = \frac{4}{d_0}\left[\Sigma^d + \Sigma^s\right] \tag{2.7}$$

The parameter τ_0 is the time scale associated to the relaxation time of Stern layer polarization, and is controlled by the diffusion length scale – taken as the diameter of the solid grain – and the molecular diffusion coefficient of the ions in the Stern layer,

$$\tau_0 = \frac{d_0^2}{8D_i^s} \tag{2.8}$$

The diffusion coefficient D_i^s is in turn related to ionic mobility μ and to temperature via the Nernst-Einstein relationship, $D_i^s = K_b T \mu_i^s/(z_i e)$, where z_i is the valence of i-th species and e the electron's charge. It is important to note that, as opposite to the assumption of (Leroy and Revil, 2009a; Revil and Florsch, 2010), mobility (and thereof diffusivity) of ions in the Stern layer is likely to be smaller (due to electrostatic interactions) than in the bulk fluid. To model the frequency dependent conductance of the Stern layer, the approach described by (Leroy and Revil, 2009a; Revil and Florsch, 2010) was adopted. The in-phase and quadrature components were computed as

$$\Sigma^{s*}(\omega) = \Sigma^{s'} + i\Sigma^{s''} \tag{2.9}$$

$$\Sigma^{s'}(\omega) = \Sigma^s\left(1 - \int_0^\infty \frac{g(\tau)}{1+\omega^2\tau^2}d\tau\right) \tag{2.10}$$

$$\Sigma^{s''}(\omega) = \Sigma^s \int_0^\infty \frac{g(\tau)\omega\tau}{1+\omega^2\tau^2}d\tau \tag{2.11}$$

where $g(\tau)$ is the distribution of relaxation times, and it is related to the grain size-distribution of the porous material. For a log-normal distribution f of grain diameters d with mean d_{50} and standard deviation σ_g,

$$f(d) = \frac{1}{\sqrt{2\pi}\hat{\sigma}d}\exp\left[-\frac{(\ln(d) - ln(d_{50}))^2}{2\hat{\sigma}^2}\right] \tag{2.12}$$

where $\hat{\sigma} = \ln(\sigma_g)$ and the associated distribution of relaxation times is (Revil and Florsch, 2010),

$$g(\tau) = \frac{1}{\sqrt{8\pi}\hat{\sigma}\tau}\exp\left[-\frac{\ln(\tau/\tau_0)^2}{\sqrt{8}\hat{\sigma}}\right] \tag{2.13}$$

The characteristic relaxation time associated to grain polarization is controlled by the median grain diameter corrected by a tortuosity factor,

$$\tau_0 = \frac{\alpha d_{50}^2}{8D_i^s} \tag{2.14}$$

with $\alpha = F\varphi$. The contribution of the Stern layer to the complex surface conductance is converted into the equivalent surface conductivity (again of the Stern layer only)

$$\sigma_s^{*S}(\omega) = 4\Sigma_h\left(\Sigma^{s'} + i\Sigma^{s''}\right) \tag{2.15}$$

using the reciprocal of the expected grain size from the log-normal distribution,

$$E_h = \exp\left(\frac{\hat{\sigma}}{2} - \ln\left(d_{50}\right)\right) = \frac{1}{d_{50}} \exp\left(\frac{\hat{\sigma}}{2}\right) \tag{2.16}$$

2.1.2 Membrane Polarization

The membrane polarization mechanism assumes that the porous medium can be conceptualized as a sequence of ion-selective zones, where the pore-throats have an active role and the the pore bodies act as passive zones (Marshall and Madden, 1959; Fridrikhsberg and Sidorova, 1961). The ion-selectivity of each pore is expressed through the transport (or transfer) numbers, t^+(cations) and t^-(anions). In passive zones, both positive and negative ions transport the electrical current, and $\Delta t^{\pm} = |t^+ - t^-| = 0$. But in the active zones $\Delta t^{\pm} \neq 0$ giving rise to the accumulation of charge. Marshall and Madden (1959), parting from the equations that describe the ion flow in the presence of an electric field, solved the differential equations related to a 1D system obtaining the impedance

$$Z(\omega) = \frac{l_1}{\mu_1^+ c_o F} \times \left[t_1^+ + \frac{B}{A} + \frac{(T_2 - T_1)^2}{\dfrac{X_1(\omega) S_1}{(t_2^+)^2 t_1^+ \tanh(X_1(\omega))} + \dfrac{A}{B} \dfrac{X_2(\omega) S_2}{(t_1^+)^2 t_2^+ \tanh(X_2(\omega))}} \right] \tag{2.17}$$

where the subscript 1 denotes the passive zone and subscript 2 the active zone. l_i is the length of the pore (see figure 2.1). $\mu_i^{\pm}$ is the ionic mobility of the cations or anions, and

$$\begin{aligned} X_i(\omega) &= \left(\frac{i\omega}{2 D_i^+ t_i^-}\right)^{1/2} \frac{l_i}{2} & D_i^{\pm} &= K_b T \mu_i^{\pm} / (z_i e) \\ A &= \frac{l_1}{l_2} & B &= \frac{D_1^+}{D_2^+} \\ C &= \frac{D_1^-}{D_2^-} & T &= \frac{t_1^-}{t_2^-} \end{aligned} \tag{2.18}$$

The impedance can be rewritten (see [2] for derivation) as

$$Z(\omega) = Z_{dc}\left[1 - \eta_0 \times \left(1 - \frac{l_1/\tau_1 + l_2/\tau_2}{\dfrac{l_1}{\tau_1}\sqrt{i\omega\tau_1}\coth(i\omega\tau_1) + \dfrac{l_2}{\tau_2}\sqrt{i\omega\tau_2}\coth(i\omega\tau_2)}\right)\right] \tag{2.19}$$

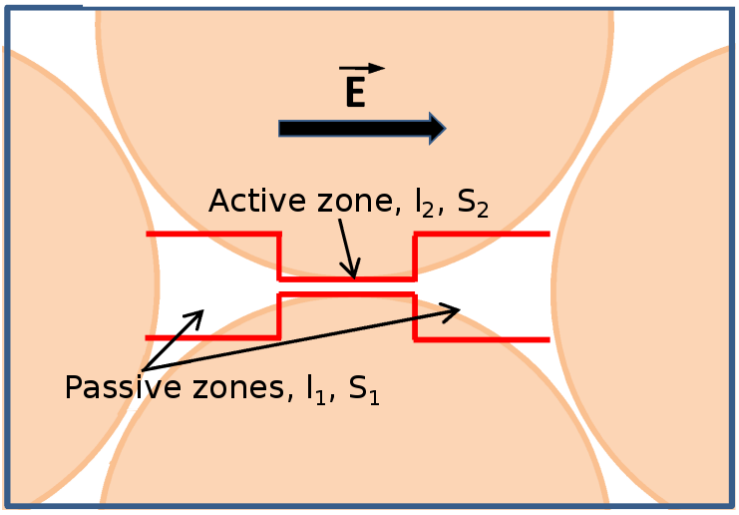

Figure 2.1: Geometrical factors for the SNP model. The passive zones (with length l_1 and cross section S_1) corresponds to the pore bodies, whereas the constriction connecting two pore-bodies (pore-throat) is the ion-selective channel, with dimensions l_2, S_2 (length and cross-section).

where

$$\tau_i = \frac{l_i^2}{8D_i^+ t_i^-} \tag{2.20}$$

$$\Upsilon = \frac{8(t_2^n t_1^+ - t_1^n t_2^+)^2}{l1/\tau_1 + l2/\tau_2} \tag{2.21}$$

$$Z_{dc} = \frac{K_b T}{ec_o F}\left[\frac{l_1}{D_1^+ + D^n + 1} + \frac{l_2}{D_2^+ + D_2^-} + \Upsilon\right] \tag{2.22}$$

$$\eta_0 = \frac{K_b T}{ec_o F}\frac{\Upsilon}{Z_{dc}} \tag{2.23}$$

$$t_i^{\pm} = \frac{\mu_i^{\pm}}{\mu_i^+ + \mu_i^-} \tag{2.24}$$

Bücker's short narrow pore model

Titov (Titov et al., 2002) developed a model assuming that the length of the passive zone is much greater than that of the ion-selective channel, and that the ionic mobilities in 1 and 2 are equal or very close ($B = C = 1$). This means that the difference in transport number is due to the difference of ionic concentration between the two zones. This difference is caused by the ionic cloud (or diffuse layer) atracted to the surface charge. Since the size of the diffuse layer is related to the Debye length of the solution, the model has to account for the size of the pore neck relative to the Debye length. This model is called the short narrow pore (SNP) model.

Bücker [2] proposed two models for membrane polarization that are a simplification of the Marshall model: the long and short narrow pore models. In

contrast to Titov's model [43] it is assumed that the anion mobility in the active zone is lower than the cation mobility following the rule

$$\mu_1^+ \approx \mu_2^+ \approx \mu_1^- \gg \mu_2^- \tag{2.25}$$

which is caused by the increased anion concentration in the active zone. It is further assumed that $A \gg 5 \cdot C$ (see 2.18). From equation 2.17 it is obtained (see [2] for the derivation)

$$Z(\omega) = Z_{dc}\left[1 - \eta_0\left(1 - \frac{1}{1+\sqrt{i\omega\tau'}}\right)\right] \tag{2.26}$$

$$\tau' = \tau_2 \frac{D_1^+ t_1^-}{D_2^+ t_2^-} \tag{2.27}$$

where Z_{dc} and η_0 are given by equations 2.22 and 2.23, and the transport numbers by equation 2.24. To account for the tortuosity as it was done in the Stern layer polarization, l_2 must be substituted by αl_2 in equations from 2.19 to 2.24. Assuming that the only factor affecting the frequency dependance of the conductivity of the solution in the porous media is the membrane polarization mechanism

$$\sigma_{\mathrm{w}}^*(\omega) = \sigma_{\mathrm{w}}^0\left[1 - \eta_0\left(1 - \frac{1}{1+\sqrt{i\omega\tau'}}\right)\right]^{-1} \tag{2.28}$$

Notice that in this case it was assumed that membrane conductivity affects the concentration of ions in the bulk pore-fluid, and not in the vicinity of the surfaces, and thereof modifies the electrical conductivity of the pore-water rather than surface conductivity. This is certainly a strong assumption which deserves further investigations, as in very small capillaries the diffuse layer can significantly affect ion concentrations and the bulk conductivity. On the other hand, the typical length scale of the double layer is at most of the order of a few tens of nanometers, while small throats are of the order of a few microns. Moreover, as already assumed for EDL polarization, the diffuse layer remains connected at the scale of a REV, and therefore strong local gradients within the diffuse layer are immediately dissipated.

Bücker's model is valid for a single type of pores (with characteristic length l_2). In a real porous medium, pore-throats diameters and radii are variable, and they follow a statistical distribution. Nevertheless, it can be assumed that the size of the passive zones compared to the size of the active zones is approximately constant, and so is also the relatioship between radii and length of the pores and throats. Both assumptions where used on Titov's original model. In this case we must integrate

$$\sigma_{\mathrm{w}}^*(\omega) = \sigma_{\mathrm{w}}^0\left[\int_0^\infty f_p(a) \times \left(1 - \eta_0(a)\left(1 - \frac{1}{1+\sqrt{i\omega\tau'}}\right)\right) da\right]^{-1} \tag{2.29}$$

where $f_p(a)$ is the normalized statistical distribution of the pore's radii.

In Titov's model a current 'efficiency' factor in the pore-throat is used. It depends on the ratio between surface and bulk fluid conductivity. Assuming a cylindrical capillary and the Debye-Huckel linearization of the EDL, the current efficiency factor was computed (Brovelli and Cassiani, 2009, TiPM and refs therein: Bowen and Jenner, 1995; Bernabé, 1998; Xuan and Li, 2004). This

stablishes a relationship with the Stern layer mechanism through the z potential, value that is needed in the efficiency factor and that is related to the surface conductivity. This means that Titov's SNP model can be used in the mixing rule that will be put forward in the next section (as well as the long narrow pore model of Bücker), but care has to be taken to be consistent in both polarization mechanisms.

2.1.3 Mixing rule

Equations 9-11 and 2.29 describe the frequency dependent electrical conductivity of the interfaces and pore-fluid. The bulk conductivity of the porous medium depends also on the relative abundance of each phase, and the geometrical configuration of the different phases. To compute the frequency-dependent bulk electrical conductivity of the porous medium, the Hashin-Shtrickman Average (HSA) model of Brovelli and Cassiani [2010, 2011] was adopted,

$$\sigma_b^*(\omega) = HSA(\sigma_{\mathrm{w}}^*, \sigma_s^*, \varphi, S_{\mathrm{w}}, m, n) = \frac{3-\varphi}{2}\varphi^{m-1}\sigma_{HSU} + \frac{\varphi-3}{2}\varphi^{m-1}\sigma_{HSL} \quad (2.30)$$

where the complex water conductivity is computed from Eq. 2.29 and the complex surface conductivity is the sum of the diffuse and Stern layers contribution,

$$\sigma_s^* = \sigma_s^d + \sigma_s^{*S}(\omega) \quad (2.31)$$

For this latter equation, Stern layer conductivity σ_s^{*S} is computed using Eq. 2.15. The upper (HSU) and lower (HSL) Hashin and Shtrikman [1962] bounds for the electrical conductivity of a mixture of solid grains and pore fluid, with volumetric fractions $(1-\varphi)$, φ and $\sigma_{\mathrm{w}}^* > \sigma_s^*$ are given by

$$HSU(\sigma_{\mathrm{w}}^*, \sigma_s^*, \varphi) = \sigma_{\mathrm{w}}^* + \frac{\varphi}{(\sigma_s^* - \sigma_{\mathrm{w}}^*)^{-}1 + \frac{1-\varphi}{3\sigma_{\mathrm{w}}^*}} \quad (2.32)$$

$$HSL(\sigma_{\mathrm{w}}^*, \sigma_s^*, \varphi) = \sigma_s^* + \frac{1-\varphi}{(\sigma_{\mathrm{w}}^* - \sigma_s^*)^{-}1 + \frac{\varphi}{3\sigma_s^*}} \quad (2.33)$$

The HSA constitutive model relies on the assumption that at the pore level the porous medium can be idealized as a mixture of two components, with bulk properties corresponding to that of the upper and lower bound. In other words, the water phase is locally well connected (and the bulk properties are computed from the upper HS bound), while in other regions the fluid connectivity is lower and the solid phase has stronger impact (the bulk properties are computed from the upper HS bound). Brovelli and Cassiani [2010b] assumed that the two components are arranged in parallel rather than in a homogeneous isotropic mixture. For 2-phase media, the permittivity of the pore-space is that of the fluid phase filling the pore space. More generally, for unsaturated materials, the conductivity of the pore-space σ_p^* is given by the combination of the permittivity of 2 immiscible phases (water and non-aqueous phase) with σ_{w}^* and σ_{nalp}^*,

$$\sigma_p^*(\sigma_{\mathrm{w}}^*, \sigma_{nalp}^*, S_{\mathrm{w}}, n) = \mathrm{w}\sigma_{HSU}(\sigma_{\mathrm{w}}^*, \sigma_s^*, S_{\mathrm{w}}) + (1-\mathrm{w})\sigma_{HSL}(\sigma_{\mathrm{w}}^*, \sigma_s^*, S_{\mathrm{w}}) \quad (2.34)$$

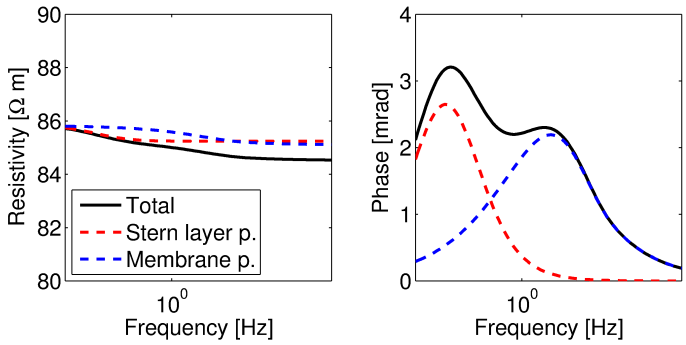

Figure 2.2: Example of model predictions obtained using the HSA-IP model. The solid black line shows the convoluted response, in terms of bulk resistivity (left panel) and phase shift (right panel). The red dashed line shows the model results when only the Stern layer polarization is considered, while the blue dashed line is relevant to the case with membrane polarization only. For this example, porosity was set to 0.39, the cementation factor to 1.85 and the D50 of the grain size distribution to 160 m.

where σ^*_{napl} is the complex electrical conductivity of the non-aqueous phase liquid (e.g. air or oil), S_w is water saturation ($0 < S_\mathrm{w} \leq 1$) and w is the weight function (defined at $\omega = 0$)

$$\mathrm{w} = \frac{\sigma^0_\mathrm{w}}{\sigma_{HSU}(\sigma^*_\mathrm{w}, \sigma^*_s, S_\mathrm{w}) S_\mathrm{w}^{-n}} \tag{2.35}$$

It is important to note that using this approach the contribution of the Stern layer is not affect by water saturation. This is physically justified, as the solid grains remain covered by a thin film of liquid water even at very low saturation, and therefore the properties of the Stern layer (which is only a few Ångström thick) are nearly unaffected. See figure 2.2 for an example of model predictions using the HSA-IP model.

2.2 Sensitivity analysis

The sensitity analysis results can be seen on figures 2.3 to 2.10. The input parameters are: the cementation factor, the conductivity of the pore water, the grain size distribution, the diffusion coefficients of the Stern and diffuse layer (related to the ionic mobility following Einstein's equation), the porosity, the conductivity of the Stern layer and the diffuse layer, the water saturation and the pore throat length distribution (see figure 2.9). The saturation index was found to have no measurable effect on the phase spectra, which is close to the results obtained by [20].

From figure 2.4 we can confirm that the smaller the grain size, the higher the frequency of the maxima of the Stern layer polarization and the higher the phase (at the same frequency) of the membrane polarization. In terms of pore

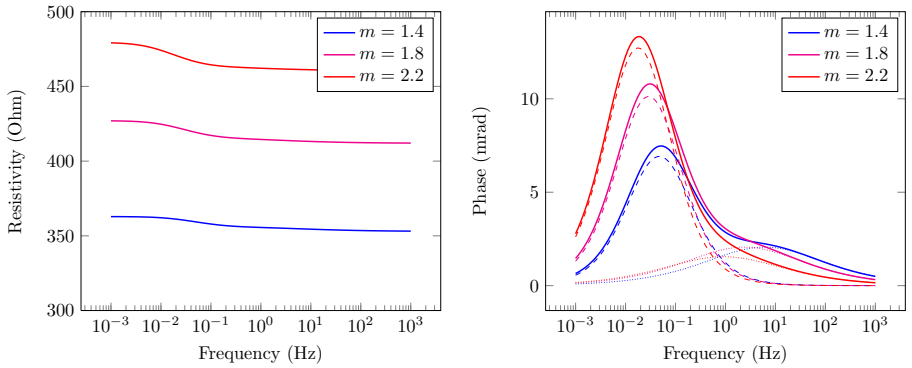

Figure 2.3: Sensitivity analysis. Cementation factor was varied between 1.4 and 2.2. The dashed line represents the Stern's layer polarization, the dotted line the membrane polarization, and the continuous line the total IP effect.

geometry, the membrane polarization mechanism is more influenced by the pore throat radius distribution as can be seen on figure 2.9.

In terms of electrochemical properties, the relatioship between the ion mobility in the Stern and diffuse layer is crucial for the membrane polarization mechanism as it was expected (figure 2.5), while the conductivity of the Stern layer played a major role in the Stern layer polarization (figure 2.8).

A lower water saturation level produces a lower membrane polarization while the Stern layer polarization increases. This is consistent with the real data (see for example figure 4.2 versus figure 4.3 and figure 4.4 versus figure 4.5). Nevertheless, the curve tends also to be flatten, which is not produced by the model and causes a higher missfit.

Unless otherwise specified, the parameters used for the sensitivity analysis were: $m = 1.85$, $n = 2.0$, $\sigma^*_{\mathrm{w}}(\omega) = 5.84 \times 10^{-2}$, $\Sigma^s = 1.85 \times 10^{-9}$, $\Sigma^d = 3.5 \times^{-8}$, the D_{50} and standard deviation of the grain size distribution were 1.6×10^{-4} and $exp(0.45)$, the pore throat radius D_{50} and standard deviation were 6.92×10^{-7} and 1.25×10^{-7}, the diffusion coefficient of the ions at the Stern layer $D_i^s = 1.5 \times 10^{-9}$ and the diffusion coefficient of cations in the diffuse layer in the active zone $D_2^- = 2.5 \times 10^{-10}$, $S_w = 1.0$, $\phi = 0.3$ and $\sigma^0_{\mathrm{w}} = 10^{-2}$;

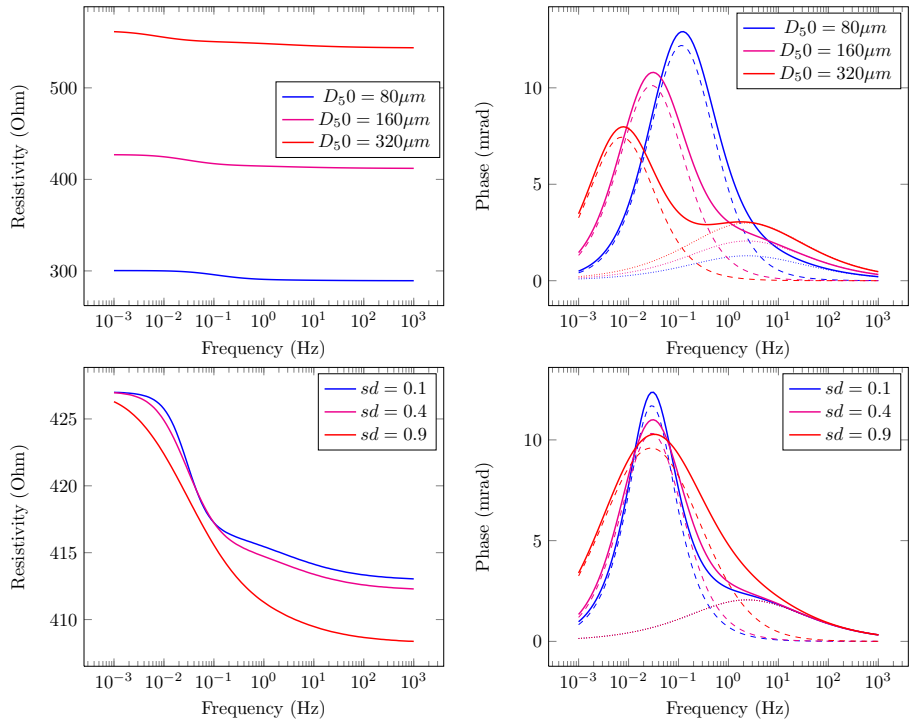

Figure 2.4: Sensitivity analysis. Effect of the grain size distribution. Top: effect of D50. Bottom: effect of standard deviation. The dashed line represents the Stern's layer polarization, the dotted line the membrane polarization, and the continuous line the total IP effect.

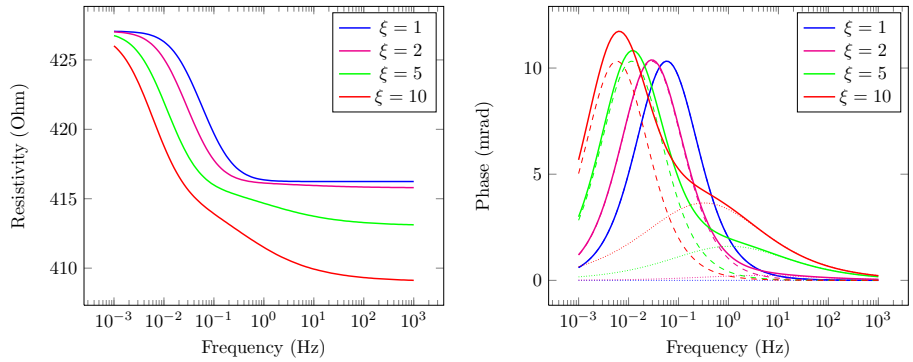

Figure 2.5: Sensitivity analysis. Effect of the ion mobility. The legend shows the ratio between mobility in the EDL and in the bulk fluid. The dashed line represents the Stern's layer polarization, the dotted line the membrane polarization, and the continuous line the total IP effect.

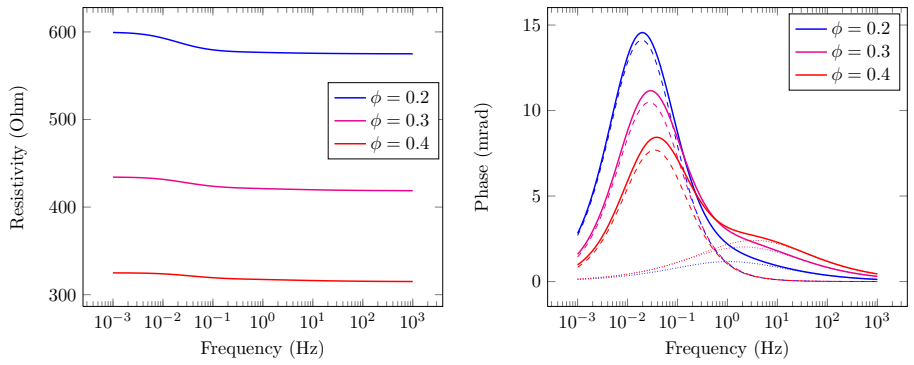

Figure 2.6: Sensitivity analysis. Porosity was varied between 0.2 and 0.4. The dashed line represents the Stern's layer polarization, the dotted line the membrane polarization, and the continuous line the total IP effect.

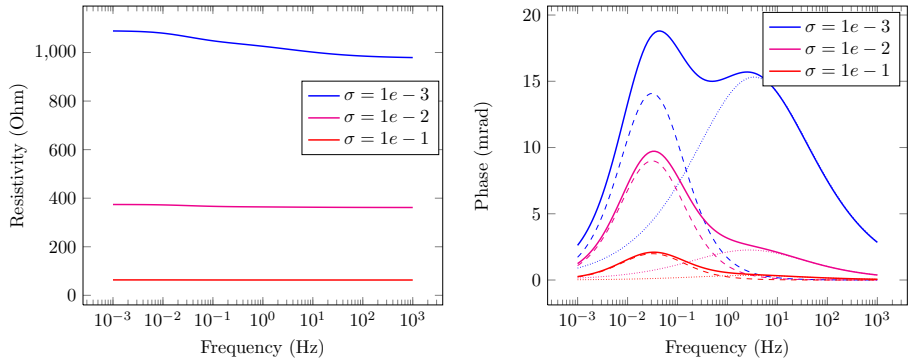

Figure 2.7: Sensitivity analysis. Effect of pore water conductivity. The dashed line represents the Stern's layer polarization, the dotted line the membrane polarization, and the continuous line the total IP effect.

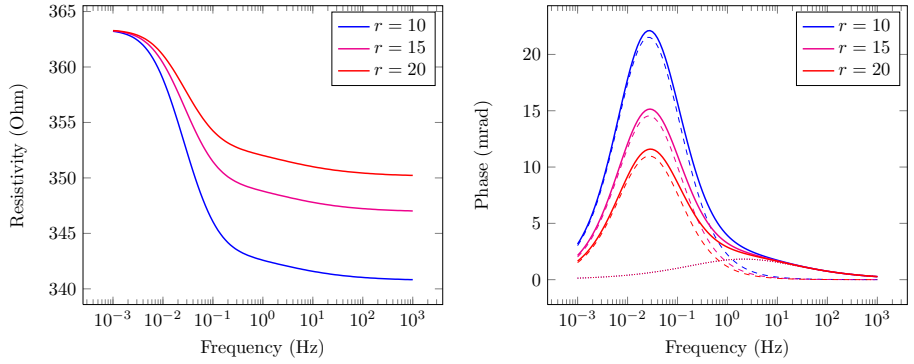

Figure 2.8: Sensitivity analysis. Effect of the conductivity of the Stern layer and the diffuse layer. The legends show the ratio r between conductivity of the Stern layer and conductivity of the diffuse layer. The dashed line represents the Stern's layer polarization, the dotted line the membrane polarization, and the continuous line the total IP effect.

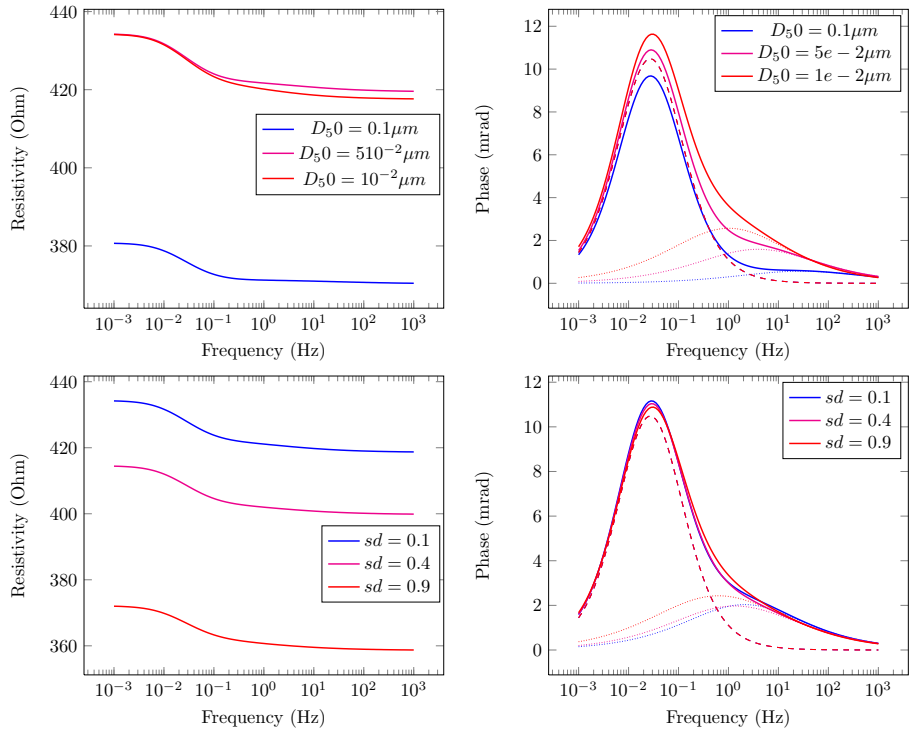

Figure 2.9: Sensitivity analysis. Effect of the throat radius distribution. Top: effect of D50. Bottom: effect of standard deviation. The dashed line represents the Stern's layer polarization, the dotted line the membrane polarization, and the continuous line the total IP effect.

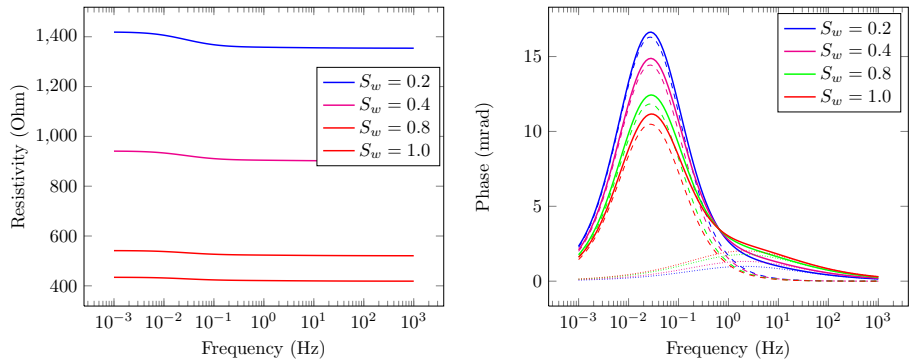

Figure 2.10: Sensitivity analysis. Effect of pore water saturation. The dashed line represents the Stern's layer polarization, the dotted line the membrane polarization, and the continuous line the total IP effect.

Chapter 3

Numerical modelling

The model described in section 2.1.2 assumes a very simple geometry of the pore space. This is so because obaining an analytical solution for more complex geometries is very difficult. The high computation capacity that is available today calls for a numerical aproximation of the phenomenon to get better insight about the origins and causes of the induced polarization. Volkmann [18] made a numerical approximation solving the case of a three dimensional cylinder with varying ionic mobilities between the passive and active zones, as well as a different ionic concentration between the electrical double layer and the rest of the fluid. As mentioned before, the equations solved are the Poisson-Nerst-Planck (PNP) equations. The numerical solution of the PNP involves the solution of a coupled system of equations: Poisson's equation to obtain the electrostatic potential based on the charge distribution, and the Nerst-Planck equation to calculates the charge distribution due to the ion flow in the presence of an electrostatic field. Both solvers are runned one after another, taking the solution of one as the input for the next until the solution of each does not varies more than an allowed threshold. This means that the coupled system can be computationally expensive to solve. This has been done with good results to calculate the electrostatic potential in ion channels (see for example [21] and [32]). To be used in spectral IP, this coupled system has to be transformed to the frequency domain and solved for each frequency. This means running two coupled numerical solvers as many times as frequencies for which a solution is obtained. This makes the process even more expensive in terms of the computing power needed. Volkmann [18] solved the coupled system using the finite element method, but with no fixed charges on the surface of the mineral due to the transformation into the complex domain to calculate the frequency-dependant impedance.

In this work we present a different approach. Before the voltage is applied, there is an electrostatic field given by the fix charges on the surface of the mineral and the ions in the pore water. This electrostatic potential can be calculated using the Poisson-Boltzmann equation, which describes precisely this situation under the assumption of thermal equilibrium. When a constant voltage is applied, even though usually a high voltage is used, the originated field in the pore space is low when compared with the field created by the fix charges close to the surface of the minerals. The assumption is made that even though there is no longer thermal equilibrium since there are moving charges, the error introduced if the Poisson Boltzmann equation is used is low.

Once the electrostatic potential for the direct current case is calculated, the complex resistivity is computed using a modified dielectric map using the electrostatic potential map obtained using the PBE. This means solving only one equation for each frequency, plus the PBE three times as it will be shown in the following sections.

3.1 The Poisson-Boltzmann equation

The Poisson-Boltzmann equation (PBE) describes the electrostatic potential in a system where fixed and free charges are present in the context of the Debye-Huckel continuum electrostatic theory ([10]). From Gauss law and the definition the electrostatic potential Φ it can shown that

$$\nabla \cdot (\epsilon_d(\mathbf{x})\nabla\Phi(\mathbf{x})) + \rho_f(\mathbf{x}) = 0 \tag{3.1}$$

where ϵ_d is the dielectric permitivity of the material -and is not assumed to be constant- and ρ_f is the total free charge density. We may now divide the free charge density between fixed ρ^f and solvent ρ^s, so that the equation becomes

$$\nabla \cdot (\epsilon_d(\mathbf{x})\nabla\Phi(\mathbf{x})) + \rho^f(\mathbf{x}) + \rho^s(\mathbf{x}) = 0 \tag{3.2}$$

this equation governs the electrostatic field due to charges in -or close to- a solvent with ions. The ions in the solvent have an electrostatic energy given by

$$U_e(\mathbf{x}) = q_i\Phi(\mathbf{x}) = ez_i\Phi(\mathbf{x}) \tag{3.3}$$

where e is the electron's charge, and z_i is the valence of the ion. Since this energy takes discrete values, and because it's microscopic nature, at thermic equilibrium the concentration $c_i(\mathbf{x})$ of ions of charge $q_i = ez_i$ must follow a Boltzmann distribution, so that:

$$c_i(\mathbf{x}) = c_i^0 \exp\left(-\frac{U_e(\mathbf{x})}{k_BT}\right) = c_i^0 \exp\left(-\frac{ez_i\Phi(\mathbf{x})}{k_BT}\right) \tag{3.4}$$

in the presence of various type of ions the solvent charge density is given by

$$\rho^s(\mathbf{x}) = \sum_{i=1}^{n} ez_ic_i(\mathbf{x}) = \sum_{i=1}^{n} ez_ic_i^0 \exp\left(-\frac{ez_i\Phi(\mathbf{x})}{k_BT}\right) \tag{3.5}$$

which put into equation (3.2) means

$$\nabla \cdot (\epsilon_d(\mathbf{x})\nabla\Phi(\mathbf{x})) + \sum_{i=1}^{n} ez_ic_i^0 \exp\left(-\frac{ez_i\Phi(\mathbf{x})}{k_BT}\right) + \rho^f = 0 \tag{3.6}$$

taking into account that $\epsilon_d(\mathbf{x}) = \epsilon_0\epsilon(\mathbf{x})$, and normalizing to calculate the dimensionless electrostatic potential $\frac{e}{k_BT}\Phi$ we get:

$$\boxed{\nabla \cdot (\epsilon(\mathbf{x})\nabla\varphi(\mathbf{x})) = -\frac{e}{k_BT\epsilon_0}\left(\sum_{i=1}^{n} ez_ic_i^0 \exp\left(-z_i\varphi(\mathbf{x})\right) + \rho^f\right)} \tag{3.7}$$

3.1.1 Further simplifications

In the presence of only one monovalent salt, and if the concentration of negative and positive ions is the same and given by c^0 this equation can be further simplified because

$$\begin{aligned}\rho^s = ec^+(\mathbf{x}) - ec^-(\mathbf{x}) &= e\left[c^0 \exp\left(\frac{e\Phi(\mathbf{x})}{k_B T}\right) + c^0 \exp\left(-\frac{e\Phi(\mathbf{x})}{k_B T}\right)\right] \\ &= -2ec^0 \sinh\left(\frac{e\Phi(\mathbf{x})}{k_B T}\right)\end{aligned} \tag{3.8}$$

which if normalized and substituted in (3.7) results in

$$\nabla \cdot (\epsilon(\mathbf{x})\nabla\varphi(\mathbf{x})) = \frac{e}{k_B T \epsilon_0}\left(2c^0 \sinh\varphi(\mathbf{x}) - \rho^f\right) \tag{3.9}$$

and defining $\gamma \equiv \dfrac{2ec^0}{k_B T \epsilon_0}$ and $\rho_n^f \equiv \dfrac{e}{k_B T \epsilon_0}\rho^f$

$$\boxed{\nabla \cdot (\epsilon(\mathbf{x})\nabla\varphi(\mathbf{x})) - \gamma \sinh\varphi(\mathbf{x}) = -\rho_n^f} \tag{3.10}$$

a linear approximation can be made on (3.6) noting that if $q_i\Phi(\bar{r}) \ll k_B T$ the exponential function can be approximated by

$$\exp\left(-\frac{ez_i\Phi(\mathbf{x})}{k_B T}\right) \approx 1 - \left(\frac{ez_i\Phi(\mathbf{x})}{k_B T}\right) \tag{3.11}$$

so that equation (3.6) now becomes

$$\nabla \cdot (\epsilon_d(\mathbf{x})\nabla\Phi(\mathbf{x})) + \sum_{i=1}^{n} ez_i c_i^0 - \sum_{i=1}^{n}\left(\frac{(ez_i)^2 c_i^0 \Phi(\mathbf{x})}{k_B T}\right) + \rho^f = 0 \tag{3.12}$$

if the solution is neutral, then $\sum_{i=1}^{n} ez_i c_i^0 = 0$, and taking into account that $\epsilon_d(\mathbf{x}) = \epsilon_0\epsilon(\mathbf{x})$, we get

$$\nabla \cdot (\epsilon_d(\mathbf{x})\nabla\Phi(\mathbf{x})) - \left(\sum_{i=1}^{n} \frac{(ez_i)^2 c_i^0}{\epsilon_0 k_B T}\Phi(\mathbf{x})\right) + \rho^f = 0 \tag{3.13}$$

which leads to the definition of the Debye length

$$\lambda_D = \sqrt{\frac{\epsilon_0 k_B T}{\sum_{i=1}^{n}(ez_i)^2 c_i^0}} \tag{3.14}$$

so that the lineal Poisson-Boltzmann equation is

$$\boxed{\nabla \cdot (\epsilon_d(\mathbf{x})\nabla\Phi(\mathbf{x})) - \lambda_D^{-2}\Phi(\mathbf{x}) + \rho^f = 0} \tag{3.15}$$

3.1.2 The boundary conditions

The algorithm used for the solution of the Poisson, Poisson-Boltzmann and complex Poisson's equation were parallelized and use the same structure. For

a detailed explanation of the numerical solution see apendix A. For the sake of simplicity only the boundary conditions are exposed here.

In order to solve the differential problem of interest, i.e. the (quasi-) steady state IP, the PBE must be equipped with suitable boundary conditions. The first aspect to consider is the need to charge the system. This means that we must add to the model the electrostatic potential generated by an external electrostatic field. The entire domain is a three-dimensional block surrounded by six faces and the field is parallel to one of the principal axes.

Two things are needed to set up the boundary conditions. The magnitude of the field, which translates as a voltage difference between the oppposite faces perpendicular to it, and the value of the potential or the ionic concentration in one point. We further assumed that the boundaries are far away enough from the object of study so that the potential generated by it is zero. This meant that:

1. Each of the two faces that are perpendicular to the field have a constant potential.

2. The potential between this two faces was updated every certain number of iterations. This was done by using the average value at the grid points closest to the opposite boundary, and adding to the boundary the potential needed to achieve the desiered voltage.

3. The other four faces (in the 3D space) are symmetric with respect to the opposite ones. The value at each boundary point was updated using the value closest to the opposite boundary point.

if no external field was applied, the electrostatic potential at the boundaries was assumed to be zero. For the sake of simplicity the voltage was applied by assuming that the value at the first face perpendicular to the field was $-V/2$ where V is the applied voltage.

Once the PBE equation is solved, a numerical solver of the complex Poisson's equation was used to calculate the impedance of the system.

3.1.3 Eliminating the noise

When the boundary conditions are applied, an ionic cloud is generated at the plates of the capacitor. This ionic cloud can mask the electrostatic potential caused by the fixed charges on the mineral and the polarization caused by the field. For the matter at hand, this is noise that has to be eliminated.

The plates of the capacitor will accumulate a charge Q. The amount of charge acumulated is straighforward if the capacitance C of the capacitor is known. In our case there is an ionic solution with an object of arbitray geometry in the solution, so the situation is more complex. Nevertheless we can calculate the total charge *inside* the capacitor using Gauss's law

$$Q_i = \epsilon_o \epsilon_r \int_{\partial\Omega} \left(\bar{E} \cdot \bar{n}\right) da \tag{3.16}$$

where $\bar{E}$ is the eletrical field, Q_i is the charge inside the capacitor, ϵ_o and ϵ_r are the vacuum permittivity and relative dielectric constant respectively, $\partial\Omega$ is a surface that surrounds the dielectric with volume Ω but without touching the

capacitor's plates and $\bar{n}$ is a unitary vector normal to $\partial\Omega$. Since $\bar{E} = -\nabla\Phi$ we can calculate the accumulated charge inside the capacitor from the solution of the PB equation as

$$Q_i = -\epsilon_o \epsilon_r \int_{\partial\Omega} (\nabla\Phi \cdot \bar{n})\, ds \tag{3.17}$$

which in the case of a discretized cuboid can be approximated as the sum along the six faces f of the cuboid of the derivative of Φ in the direction of the normal to each face times $-\epsilon_o \epsilon_r dx^2$. If Ω_f corresponds to the set of grid points that belong to the face f, the duplet (f, i) the $i-th$ grid point that belongs to Ω_f and $(f, i-1)$ the previous grid point to (f, i) in the direction of the normal to f, this can be written as

$$Q_i = -\epsilon_o \epsilon_r \left[\sum_{f=1}^{6} \sum_{i \in \partial\Omega_f} (\Phi_{f,i} - \Phi_{f,i-1}) \right] dx \tag{3.18}$$

The charge Q_i is a usefull magnitude, but it takes into account the noise we are trying to eliminate. Now note that Q_i can be divided as the sum of the fixed charges Q_f on the surface of the pore and the free ions Q_s in the solution. In the presence of an external field, the number of ions will change due to the charges Q_r that redistribute around the pore due to the change of the electrostatic potential plus the ions Q_b that accumulate at boundary due to the field. This means that

$$Q_t = Q_f + Q_s + Q_r + Q_b \tag{3.19}$$

Strictely speaking Q_r is not a polarization charge, but the difference on the total charge of the system due to the redistribution of the ions around the pore.

We can approximate the value of $Q_f + Q_s + Q_r$ by running two simulations and calculating the charge inside each system:

1. The pore is charged and the field is applied so the total charge is $Q_1 = Q_f + Q_s + Q_r + Q_b$.
2. The pore is not charged and field is applied so the total charge is given by $Q_2 = Q_b$.

In this way,

$$Q_f + Q_s + Q_r = Q_1 - Q_2 \tag{3.20}$$

Since Q_i is an integral operation, instead of calculating the integral on each the solutions given at the previous list, the difference between the simulations could be calculated and the integral applied on the resulting potential. This is correct analytically, and was also tested numerically with excellent results. In this way, two simulations need to be carried out as before

1. To obtain Φ_1 the pore is charged and the field is applied.
2. To obtain Φ_2 the pore is charged but no field is applied.

then

$$\Phi_r = \Phi_1 - \Phi_2 \tag{3.21}$$

where this electrostatic potential does not have the ionic cloud at the plates of the capacitor.

3.2 Poisson in the complex plane

Let us now consider a medium presenting both lossy dielectric and conductive components immersed in a sinusoidally oscillating electric field at the angular frequency ω. For sake of simplicity the presence of fixed charged is neglected. By means of the phasor representation the Poisson equation, which relates the electrostatic potential to the values and distribution of the complex dielectric function takes the following form:

$$\nabla \cdot \left(\mathring{\varepsilon}_{(\mathbf{x},\omega)} \nabla \mathring{\mathbf{\Phi}}_{(\mathbf{x},\omega)} \right) = 0 \tag{3.22}$$

where $\mathring{\mathbf{\Phi}}$ is a the electrostatic potential phasor and $\mathring{\varepsilon}_{(\mathbf{x},\omega)}$ is the complex permittivity given by $\mathring{\varepsilon} = \varepsilon_{eff} - j\sigma_{eff}/\omega$, ε_{eff} and σ_{eff} being the effective permittivity and conductivity, as detailed below. The boundary conditions used are: (a) periodic boundary conditions on the faces parallel to the electric field, and (b) a sinusoidal voltage imposed between the two faces perpendicular to the field. This differential problem can be solved by a finite-difference scheme in a cubic domain after space discretization and mapping of the permittivity on the derived lattice.

3.2.1 Input parameters.

The input parameters are the permittivity functions of the water and the mineral(s) present. As a first model, the following expression of water's permittivity was used:

$$\mathring{\varepsilon}^w = \varepsilon_0 \varepsilon^w_{rel} - j\frac{\sigma^0_w}{\omega} \tag{3.23}$$

where ε^w_{rel} is the static relative water permittivity, and σ_w is the static water conductivity for a given salt concentration. The permittivity of the minerals can estimated from the literature.

The static relative permittivity is usually taken close to 80. Nevertheless, for low frequencies, there is new experimental data that suggests that the permittivity of water behaves more like a non continuous function with incredible high values as the angular frequency approaches zero [5, 36]

$$\varepsilon^w_{rel} = \begin{cases} 80 & \omega \leq 0 \\ 2.4 \cdot 10^3 & \omega \to 0 \end{cases} \tag{3.24}$$

this has also been found in biological tissues, which have a very important quantity of water [15]. This is particularly important in the brain, which is mostly water [27]. In the last case the high values (close to 10^{10}) could be explained by the electrical properties of the neurites. In [5, 36] the effect of the ionic cloud on the electrodes when the measure was taken could explain the high values [6] (could be as high as $1 \cdot 10^7$ for 1Hz). Even though non polarizing electrodes are now common when measuring IP, even low salt concentrations with a small polarization on the electrodes can increase the measured static relative permittivity. In our case using a value higher than 80 was determinant. The best results were obtained using a value of $\varepsilon^w_{rel} = 2.4 \cdot 10^3$.

The conductivity of an ionic solution is given by:

$$\sigma^0_w = \sum_i n_i e Z_i \mu_i \tag{3.25}$$

where n_i is the number of charge carriers per unit volume, μ_i the mobility, Z_i the valence for the ionic species i in the electrolyte and e is the electronic charge. This means it is possible to assign different conductivities at different points of the finite difference grid used for the numerical solution according to ionic mobility. Both the numerical results of Volkmann [18] and the "new" short narrow pore model of Bücker [2] use a region with lower anionic mobility whose thickness is given by the Debye length of the solution and is adjacent to the mineral's surface. It is important to note that in complex geometries there is no reason for the diffuse layer to have constant thickness. Think of the electrostatic potential at corners, close angles or sharp tips. In our case, since we have the electrostatic potential for the continuous current case (calculated using formula 3.21), we assumed that the zones with an electrostatic potential greater than certain threshold -thus closer to the mineral's surface- had such a decreased anionic mobility. The threshold potential was arbitrarily taken as the potential caused by a point charge and a distance of one Debye length. This is a strong assumption, since probably the right thing would be to use a function of the potential and not a discrete arbitrary value. Nevertheless this matter requires further study since is not clear what function should be used.

3.2.2 Impedance calculation

From the solution of Eq. 3.22, the impedance $\mathring{\mathbf{Z}}$ can be calculated. Complex current density $\mathbf{J}$ due to conduction is given by

$$\mathring{\mathbf{J}}_{cond} = \sigma^* \mathring{\mathbf{E}} \tag{3.26}$$

while the displacement current is given by

$$\mathbf{J}_{disp} = j\omega \mathring{\mathbf{D}} = j\omega\varepsilon^* \mathring{\mathbf{E}} \tag{3.27}$$

where the starred constitutive quantities are the complex conductivity and permittivity of the material (dependence on space and frequencies are omitted for simplicity)

$$\sigma^* = \sigma' + j\sigma'' \tag{3.28}$$

$$\varepsilon^* = \varepsilon' - j\varepsilon'' \tag{3.29}$$

Since we are assuming there that the convection (aka streaming) current (ion flux due to displacement of the medium) and diffusion current (caused by the local concentration gradient of the charge carriers) are zero, the total current is given by

$$\begin{aligned} \mathbf{J}_t &= \mathbf{J}_{cond} + \mathbf{J}_{disp} = \sigma^* \mathring{\mathbf{E}} + j\omega\varepsilon^* \mathring{\mathbf{E}} = \left(\sigma^* + j\omega\varepsilon^*\right) \mathring{\mathbf{E}} \\ \mathbf{J}_t &= j\omega \left(\varepsilon^* - j\frac{\sigma^*}{\omega}\right) \mathring{\mathbf{E}} = j\omega \mathring{\varepsilon} \mathring{\mathbf{E}} \end{aligned} \tag{3.30}$$

If we separate real and imaginary part of the whole dielectric function: $\mathring{\varepsilon} = \varepsilon_{eff} - j\sigma_{eff}/\omega$, we observe that:

$$\begin{aligned} \varepsilon_{eff} &= \varepsilon' + \frac{\sigma''}{\omega} \\ \sigma_{eff} &= \sigma' + \omega\varepsilon'' \end{aligned} \tag{3.31}$$

Let us define a surface $\Sigma = \sum_{i=1}^{3} \Sigma_i$ that surrounds a cuboid with one of the plates of the capacitor inside the cuboid (see a cross-section of the surface and the capacitor at figure 3.1) where:

- Σ_1 is the part of the surface parallel to the plate, outside the cuboid.
- Σ_2 are the parts of the surface that are perpendicular to the plate.
- Σ_3 is the part of the surface parallel to the plate, inside the cuboid.

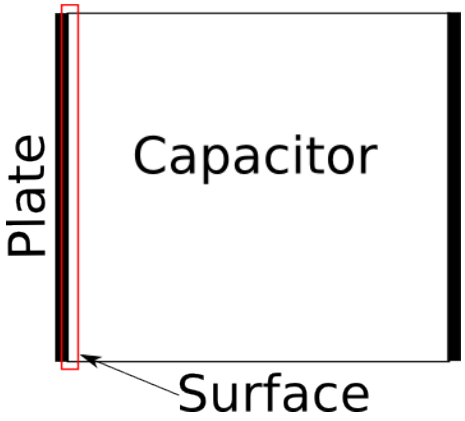

Figure 3.1

from the Divergence Theorem

$$\iiint_{\Omega} \nabla \cdot \mathbf{J}_t \, dv = \iint_{\Sigma} \mathbf{J} \cdot \mathbf{n} \, ds = \sum_{i=1}^{3} \iint_{\Sigma_i} \mathbf{J} \cdot \mathbf{n} \, ds \tag{3.32}$$

the only current that goes through Σ_1 is the conduction current that goes through the cable that feeds the capacitor, which should be equal to the total current of the circuit

$$\iint_{\Sigma_1} \mathbf{J}_t \cdot \mathbf{n} \, ds = -\mathring{\mathbf{I}} \tag{3.33}$$

assuming neglible the component of the current normal to Σ_2

$$\iint_{\Sigma_2} \mathbf{J}_t \cdot \mathbf{n} \, ds \approx 0 \tag{3.34}$$

and for the sake of simplicity let's assume that the field was applied on the direction of the $\mathbf{z}$ axis so

$$\iint_{\Sigma_3} \mathbf{J}_t \cdot \mathbf{n} \, ds = -j\omega \iint_{\Sigma_3} \mathring{\varepsilon} \mathring{\mathbf{E}}_{\mathbf{z}} \, ds \tag{3.35}$$

which means that

$$\mathring{I} = -j\omega \iint_{\Sigma_3} \mathring{\varepsilon} \mathring{\mathbf{E}} \, ds \tag{3.36}$$

so we may calculate the impedance of the system as:

$$\mathring{Z} = \frac{-\mathring{V}}{j\omega \iint_{\Sigma_3} \mathring{\varepsilon}\mathring{\mathbf{E}}\, ds} \tag{3.37}$$

it is important to notice that in the case of an homogeneous material with purely real permittivity ε and $\sigma = 0$ between the two plates (that is, a lossless insulator whose dielectric has a flat spectrum) this reduces to

$$\begin{aligned} \mathring{Z} &= \frac{j\mathring{V}}{\omega\varepsilon\mathring{E}_z A} \\ \mathring{Z} &= \frac{-j\mathring{V}}{\omega\varepsilon\mathring{\mathbf{V}} A/d} \\ \mathring{Z} &= \frac{-j}{\omega\varepsilon A/d} \\ \mathring{Z} &= \frac{-j}{\omega C} \end{aligned} \tag{3.38}$$

where A is the area of the plates and C the capacitance of a perfect capacitor, which means that the formulation is consistent with the impedance of a perfect capacitor.

3.2.3 Observing the membrane polarization

The use of a numerical method has many advantages. For example, different frequence dependant dielectric function can be used for the each dielectric, something for which currently there are no analytical models. Nevertheless, since we will have different mediums there will be Maxwell-Wagner polarization at the interface between the diverse dielectrics like the water-mineral interface. As was seen on the previous chapter the MW polarization can obscure the membrane polarization effect. To obtain results without the MW polarization obscuring the membrane polarization the real parts of all dielectrics was taken to be the same. In this case, the real part of the permittivity of water was used. An example of a result where this was done versus taking different real parts of the permittivity can be seen on figure 3.2.

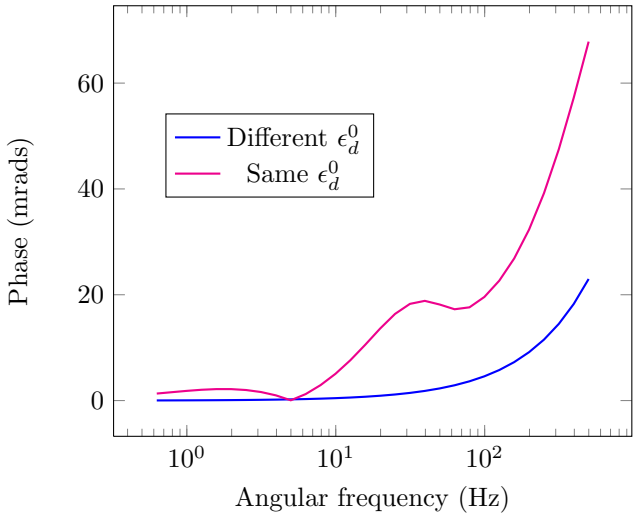

Figure 3.2: Effect of using equal or diverse real parts of the permittivity in all materials.

Chapter 4

Results

4.1 HSA model testing

The model was tested using the data from [14]. Measurements of the complex conductivity were conducted on cylindrical Plexiglas cells equipped with a four-electrode configuration. The water saturation was varied, and the porosity measured. The measured grain size distribution was fitted using a log-normal distribution. The DC resistivity was fitted using the HSA model to estimate Archie's parameters, cementation factor and saturation exponent (see figure 4.1). The high frequency component was obtained by following the procedure described in [3]. When the spectra showed a clear low frequency peak, two cole-cole curves where used. If instead it didn't only one curve was used taking into account only the data above 10Hz. The results can be seen on figures from 4.2 to 4.13. As can be seen, for full saturation (or close ot it) the results are very satisfactory except for figures 4.6 and 4.8.

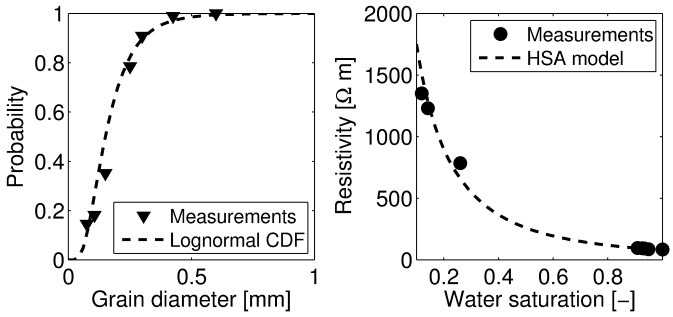

Figure 4.1: Model parameter estimation. Left panel: the measured grain size distribution was fitted using a log-normal distribution. Right panel: DC resistivity was fitted using the HSA model to estimate Archie's parameters, cementation factor and saturation exponent.

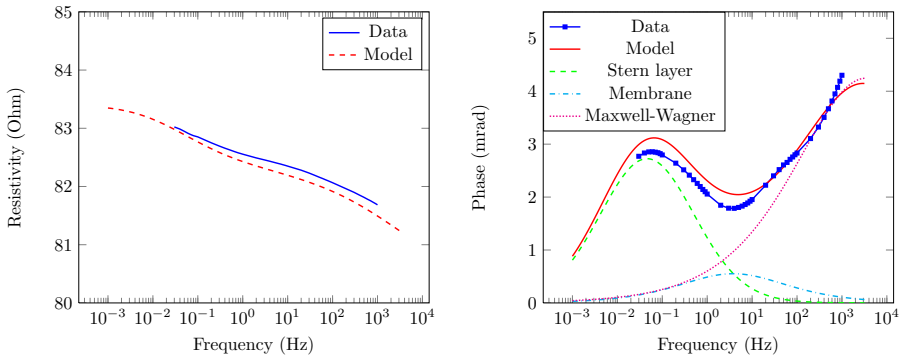

Figure 4.2: Experimental data and model predictions. Cella 1 of Cassiani et al., 2009. Saturated conditions.

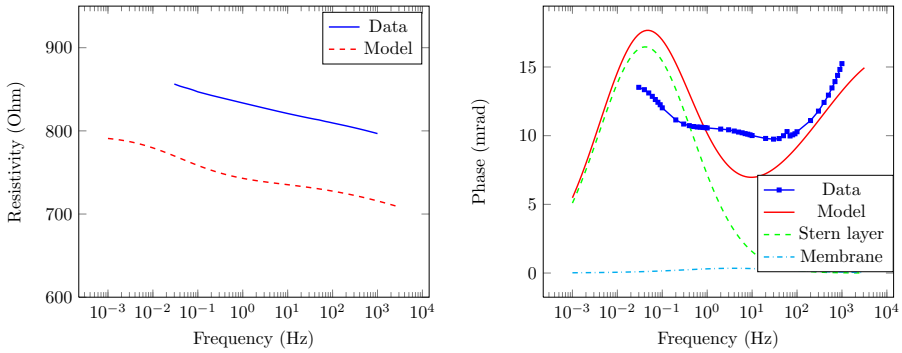

Figure 4.3: Experimental data and model predictions. Cella 1 of Cassiani et al., 2009. $S_w = 26\%$.

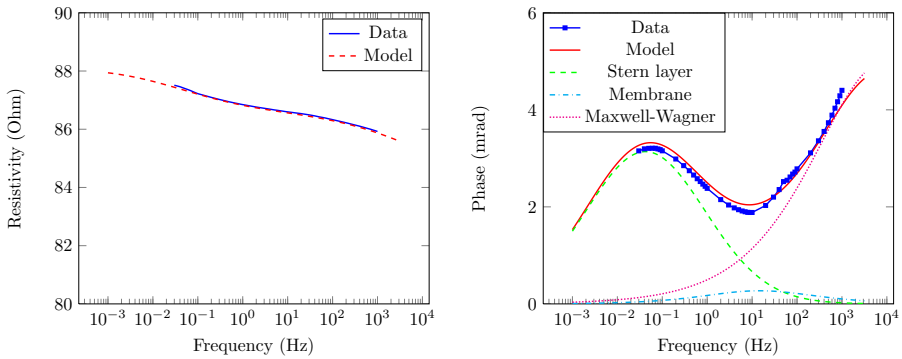

Figure 4.4: Experimental data and model predictions. Cella 2 of Cassiani et al., 2009. Saturated conditions.

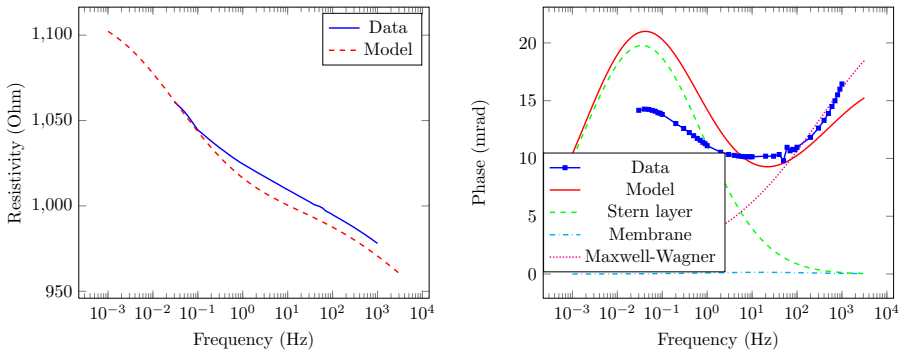

Figure 4.5: Experimental data and model predictions. Cella 2 of Cassiani et al., 2009. $S_w = 14\%$.

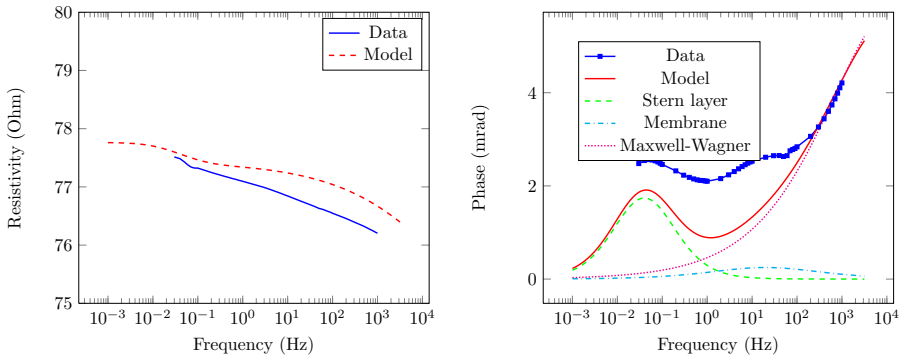

Figure 4.6: Experimental data and model predictions. Cella 3 of Cassiani et al., 2009. Saturated conditions.

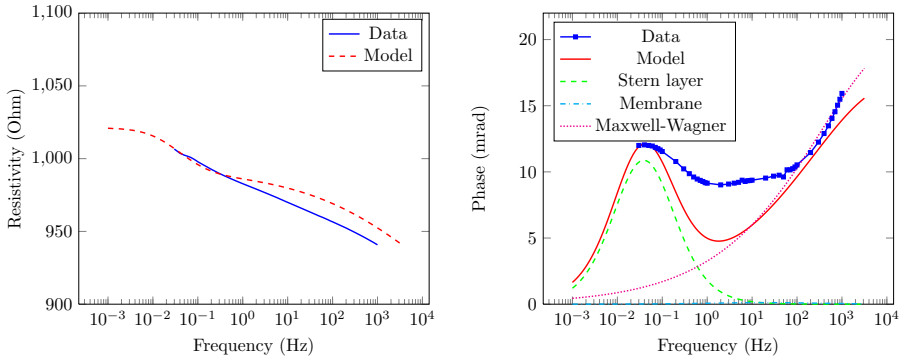

Figure 4.7: Experimental data and model predictions. Cella 3 of Cassiani et al., 2009. Saturated conditions 16%.

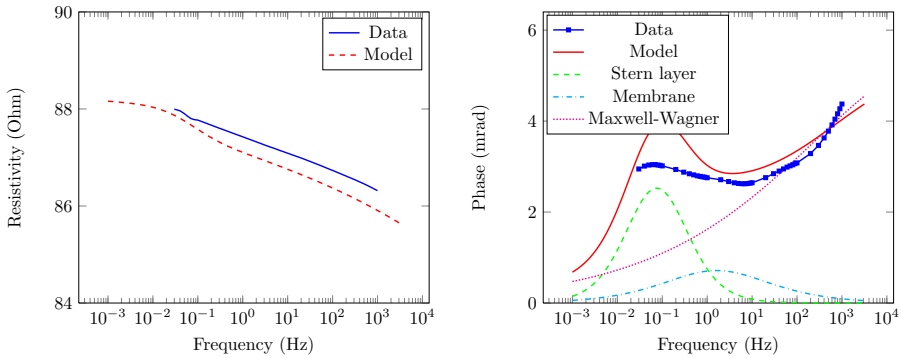

Figure 4.8: Experimental data and model predictions. Cella 4 of Cassiani et al., 2009. Saturated conditions.

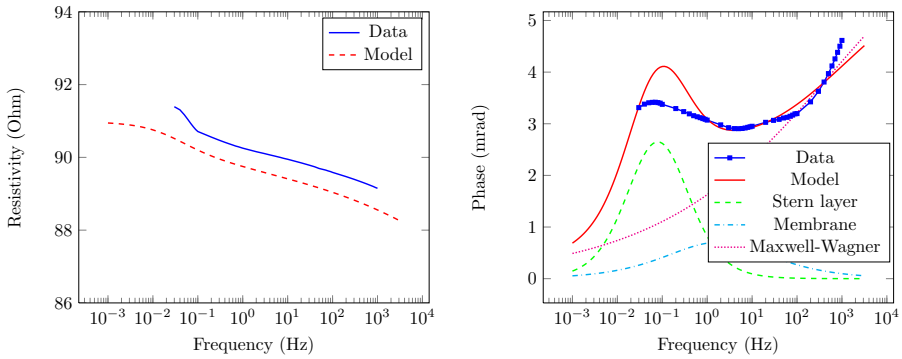

Figure 4.9: Experimental data and model predictions. Cella 4 of Cassiani et al., 2009. $S_w = 93\%$.

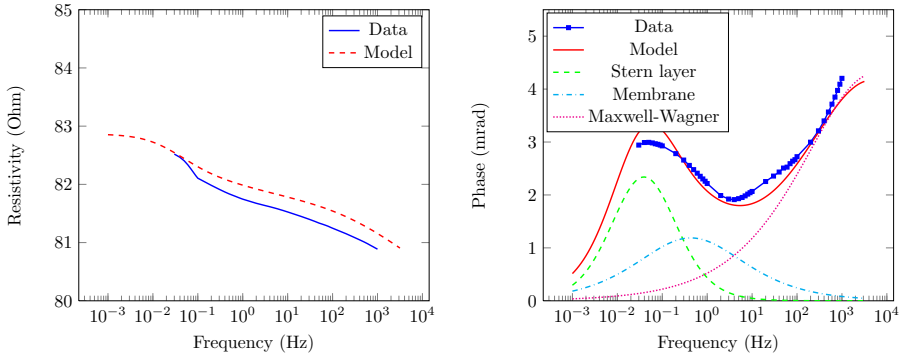

Figure 4.10: Experimental data and model predictions. Cella 5 of Cassiani et al., 2009. Saturated conditions

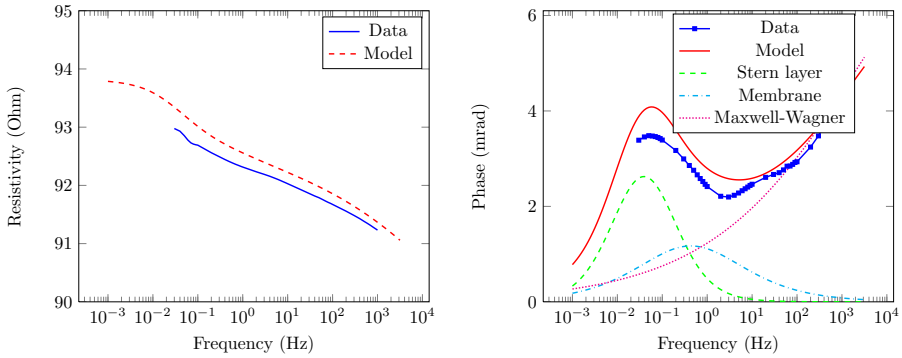

Figure 4.11: Experimental data and model predictions. Cella 5 of Cassiani et al., 2009. $S_w = 93\%$.

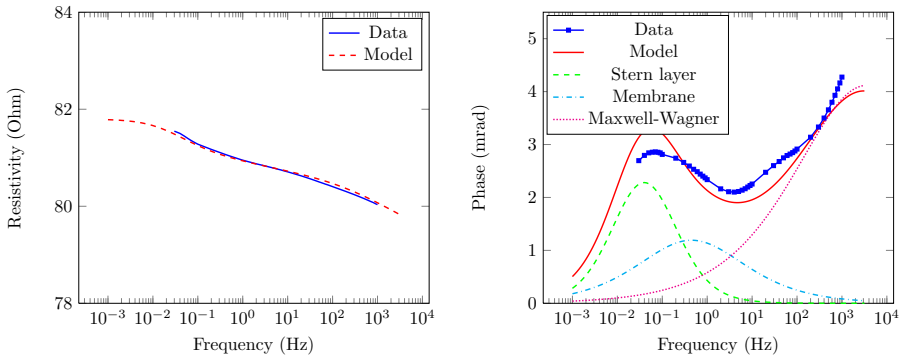

Figure 4.12: Experimental data and model predictions. Cella 10 of Cassiani et al., 2009. Saturated conditions.

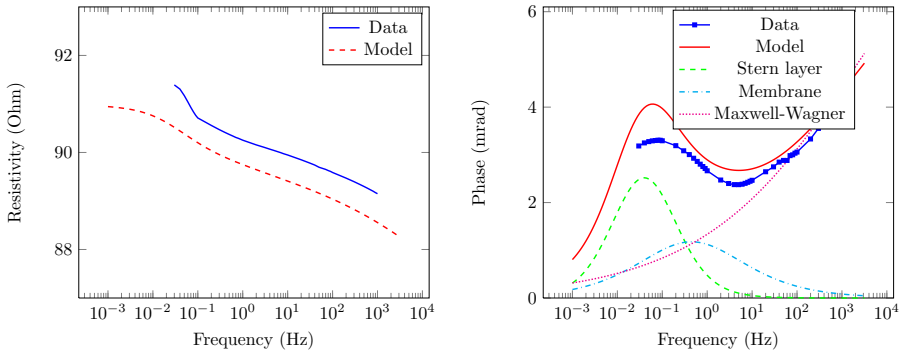

Figure 4.13: Experimental data and model predictions. Cella 10 of Cassiani et al., 2009. $S_w = 93\%$.

4.2 Numerical model testing

In figure 4.14 the precision of the solver was tested, and the impedance calculated with the solver and the analytical solution for a capacitor whose relative dielectric constant is $\varepsilon_{rel} = 80$ are plotted. In figure 4.15 you can see the phase for a capacitor with a dielectric that follows the relation $\mathring{\varepsilon} = 80\varepsilon_0 - j\sigma/\omega$.

The test of the numerical model proved to be a difficult endevour. The characteristic frequency of Bücker's new short narrow pore model is given by [2]

$$\tau_{nSNP} = (1 - \eta_0)\,\tau' \tag{4.1}$$

where τ' is given by equation 2.27 and η_0 by equation 2.23. This means that for small chargeabilities

$$\tau_{nSNP} = \frac{l_2^2}{8D_2^+ t_2^-}\frac{D_1^+ t_1^-}{D^+ 2t_2^-} \tag{4.2}$$

with the conditions that $A \gg 5C$ and $C \gg 1$. This frequency is independent of the throat radius, as long as the last conditions are met. This clearly has no physical meaning if the radius of the throats are too large which is a problem in the SNP model. Moreover, because of the last conditions, having a maximum phase shift in the frequencies where the membrane polarization could be measured (as in the last chapter) is costly from the computational point of view because the large size of the active zone. Note that the shorter the active zone, the higher the frequency of the maximum phase shift. For this reason the model was tested against the numerical results of Volkmann [18]. In it three cylinders with different radius (just as in figure 2.1). Volkmann used a layer of thickness equal to one Debye length for the low anionic mobility zone, we used the algorithm described above. The results can be seen of figure 4.16. The main difference is the high frequency component which is absent in Volkmann's data. This can be explain by the fact that Volkmann used a contant value of the permittivity of water for all frequencies. Note that the frequency corresponding to the maximum phase is very close in both graphs.

On figure 4.17 water and the mineral are substituded by vacuum to highlight the contribution of each. On figure 4.18 two different curves are shown for two different porosities. On figure 4.19 two different geometries are shown. One with 17 spheres and a very high permeability, the other is just a square filled with random water pockets which means null permeability. The difference between the two is clear, and makes perfect sense for it to be so. Also, this is where the tool -a solver like this one- is usefull.

4.3 Discussion and Conclusions

The model comparison with experimental data suggest that IP is the results of both grain and membrane polarization. The HSA model results reafirm the idea that grain polarization typically occurs at lower frequencies than membrane polarization, which may make the latter hard to be identified in real data because Maxwell-Wagner polarization and the noise at higher frequencies frequently often hide it. In addition, decoupling procedures based on Debye curve fitting can add further uncertainty since the phase shift at the lower part of the curve may due to pore throat polarization and not Maxwell-Wagner.

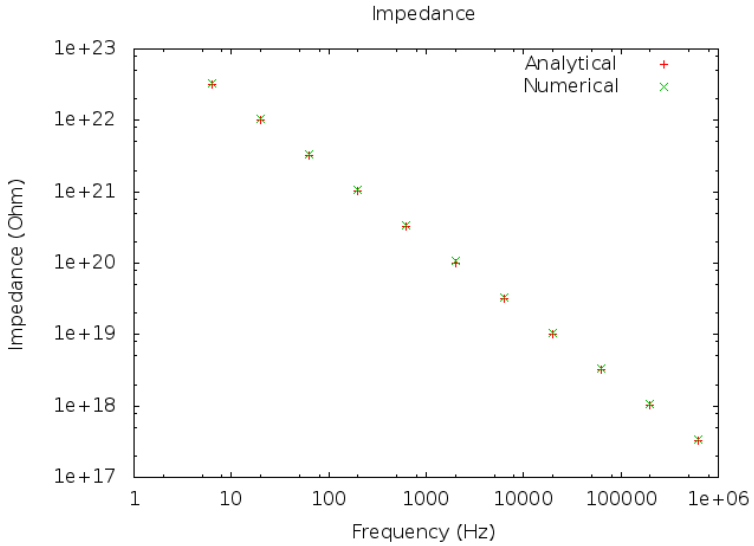

Figure 4.14: Impedance for $\varepsilon_{rel} = 80$.

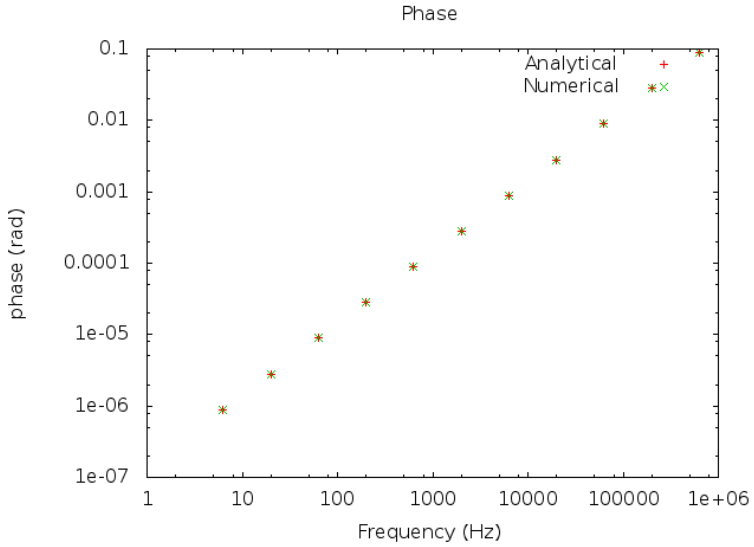

Figure 4.15: Phase for $\mathring{\varepsilon} = \varepsilon_0 80 - j\sigma/\omega$ with $\sigma = 5e - 3S/m$.

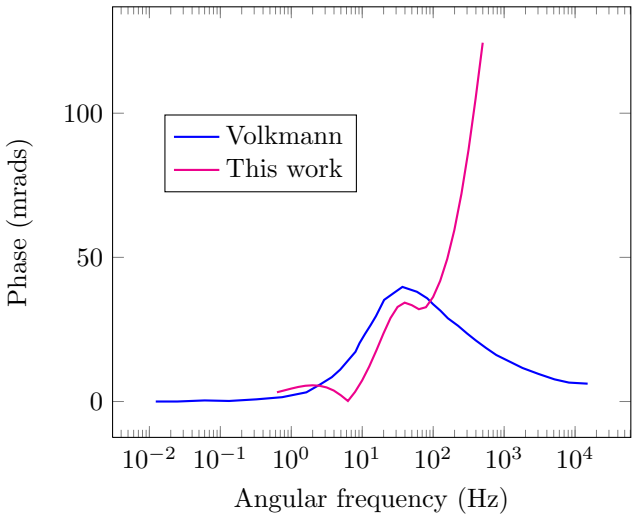

Figure 4.16: Volkmann's data.

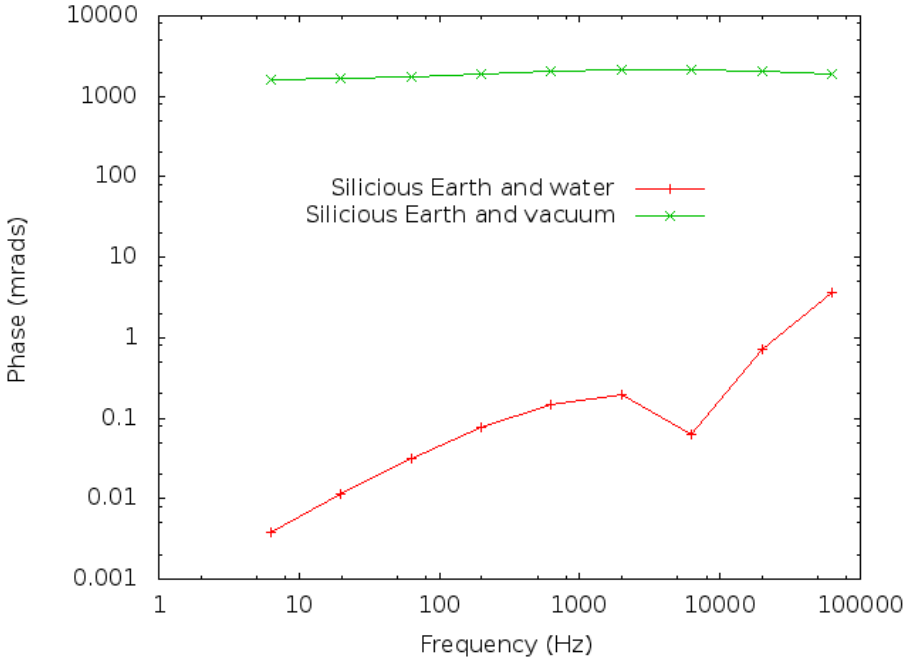

Figure 4.17: Mineral and water are substituded by vacuum

The proposed model helps to explain different types of IP response observed in the phase plots: (a) if a single peak is observed, it's either due to grain or pore-throat polarization, and therefore the associated relaxation time should be related to the corresponding characteristic length; (b) if 2 peaks are observed, the 2 components have similar contribution, and the characteristic time scales are markedly different (i.e. grain size is >> than pore-throat length); (c) if no peak is visible (the CPA model) the two time scales are similar and/or the relaxation time distributions associated to pores and grains are broad and ultimately overlap.

According to our model, as water saturation decreases, the contribution of surface conductivity (i.e of Stern layer polarization) becomes dominant, as membrane polarization is constant. This can also explain the shift of the relaxation time towards lower frequencies sometimes observed (e.g. Binley et al, 2005). At $S_w = 1$, the contribution of Stern layer and membrane polarization is similar, and the observed phase shifted (fitted with a debye distribution) is the convolution of the 2 components. As S_w decreases, the contribution of membrane polarization decreases and the phase peak moves towards lower frequencies.

The numerical methodology gave good results, which means it can be a useful tool to study the induced polarization phenomenon. The results allowed us to see the membrane polarization effect, as well as the high frequency component and a low frequency component which could be related to stern layer polarization. The numerical solver of the complex Poisson equation was particularly difficult to use because it can diverge if a wrong over-relaxation factor is used. The over-relaxation factor proved to be geometry and frequency dependent so

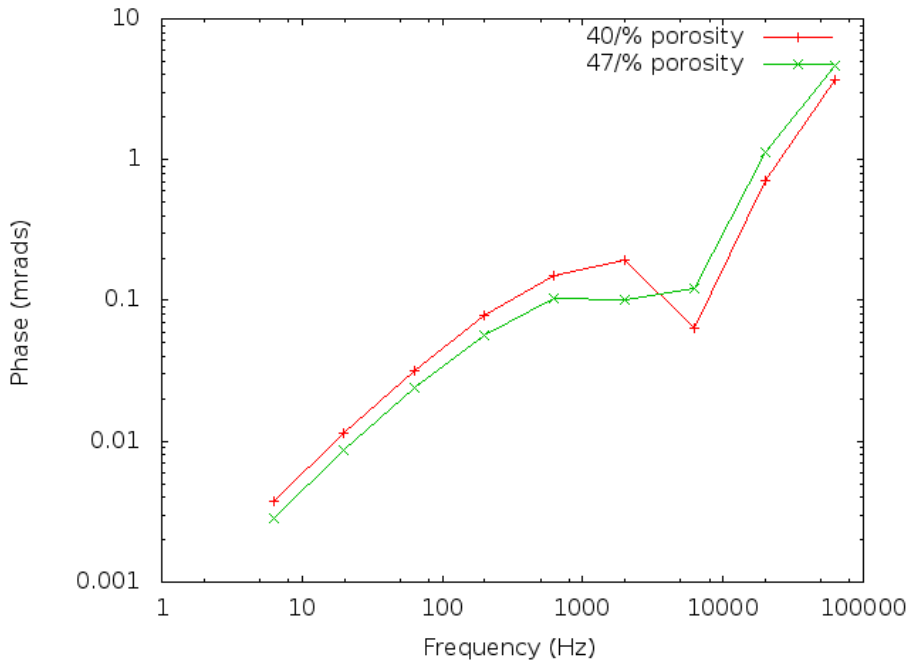

Figure 4.18: Varying porosity on Silicious Earth.

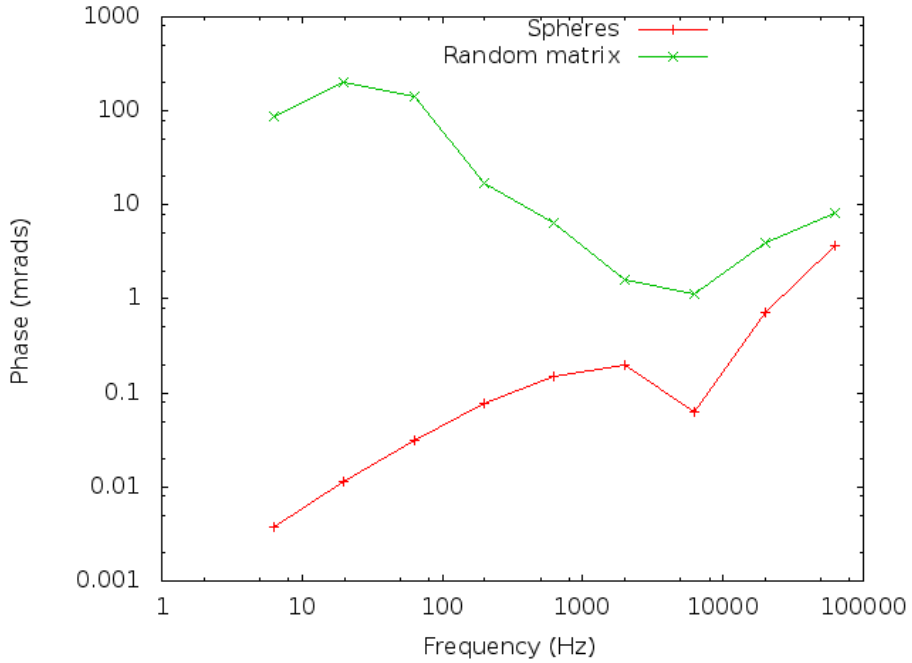

Figure 4.19: Varying geometry on Silicious Earth. Both systems have the same porosity and dielectric functions, but one has 17 spheres (one with diameter equal to the length of the box and 16 smaller spheres around) and the other a random matrix with permeability zero.

that for the same geometry different over-relaxation factors had to be used to generate the phase spectra.

Complex dielectric functions were also used to test the stability of the numerical method. There are no theoretical curves to which the results could be compared to, but the form of the curve resemble real data.

The low frequency component deserves more attention. Since periodic boundary conditions where used at the faces parallel to the applied field, the mineral's geometry is surrounded by water and could show the effect of the polarization of the Stern layer. Nevertheless we were not able to reproduce the effect on a simple sphere. This could be because the polarization of a single sphere on a cuboid is to low from only an electrical point of view. The use of complex geometries with spheres of different sizes could help to understand this.

The use of the Poisson-Boltzmann equation to delineate the region with lower anionic mobility showed promising results. Even though the factor multiplying the electrostatic potential at a distance λ from the mineral's surface was arbitrary, there is no reason to assume that this distance should be λ as it is frequently done. This means further analysis is required. For example, maybe a continuous function could be used instead of discrete one. Nevertheless, the results were encouraging as a firt approximation. Is important to notice that even though the geometries tested were not complex, the same software and methodology -at least theoretically- could be applied to more complex structures. The challenge in this case is to build such structures have a resemble the real physical world.

Appendix A

Parallelization of the finite differences solver

In this work was used an implementation of a linear PBE solver based on a Finite-Difference (FD) scheme using the Message Pasing Interface (MPI) library. We follow the approach of the DelPhi PBE solver [28, 34], which exploits the checkerboard structure of the finite difference discretization of the Laplace differential operator and adopts a Successive Over Relaxation (SOR) scheme to converge to the solution.

A.1 Sequential solution of the Poisson-Boltzmann equation

The PBE combines the continuum electrostatics description of fixed charges in a dielectric medium with the Boltzmann prescription for mobile ions in aqueous solvent at the thermal equilibrium with a reservoir [7]. In its linearized form, which is valid for low ionic concentrations, the PBE reads:

$$\nabla \cdot [\epsilon(\mathbf{x}) \nabla \Phi(\mathbf{x})] + \frac{\rho^{fixed}}{\epsilon_0} = \frac{\epsilon_{solv}}{\lambda^2} \Phi(\mathbf{x}) \tag{A.1}$$

where Φ is the electrostatic potential, $\epsilon(\mathbf{x})$ the space-varying relative dielectric constant, ϵ_{solv} that of solvent, ϵ_0 the permittivity of vacuum, ρ^{fixed} the fixed charge density on the solute, and λ is the Debye length of the ionic solution, a quantity describing the electrostatic screening induced by the ionic cloud in the solution. The right hand side of equation (3.15) is present only if $\mathbf{x}$ is located in the ionic solution. The sequential implementation described here follows the approach described in [28]. The PBE discretized on a uniform grid takes the following form:

$$\left[\sum_{i=1}^{6} \epsilon_i + \epsilon_{solv} \left(\frac{h}{\lambda} \right)^2 \right] \Phi_j - \sum_{i=1}^{6} \epsilon_i \Phi_i - \frac{q_j}{\epsilon_0 h} = 0 \tag{A.2}$$

where Φ_j refers to the electrostatic potential at the node j, where a net charge q_j is mapped. The term containing λ is present only if the node j belongs to the

solvent and ϵ_i is the relative dielectric constant at one of the midpoints between the node j and its six nearest neighbors on the grid, h is the grid spacing. This discretized relationship leads to a linear system of equations $A\mathbf{\Phi} = \mathbf{b}$ where a suitable mapping converting three dimensional to one dimensional indexes has to be adopted. The matrix A can then be decomposed into $A = D + L + U$, where D is the diagonal of A, U and L are the strict upper and lower triangular parts of A, respectively. According to the Successive Over-Relaxation method, the iterative equation is given by:

$$\mathbf{\Phi}^{(n+1)} = (D + \omega L)^{-1} \left\{ \omega \mathbf{b} - [\omega U + (\omega - 1)D] \, \mathbf{\Phi}^{(n)} \right\} \tag{A.3}$$

where ω is the over-relaxation factor and bracketed superscripts indicate iteration number. The term $(D + \omega L)^{-1}$ can be calculated using forward substitution since $D + \omega L$ is a lower triangular matrix implying that the iterative scheme must be consistent with the previously described mapping, which makes parallelization difficult. The iteration stencil becomes:

$$\Phi_j^{(n+1)} = \omega \left(\frac{\sum_{i=1}^{6} \epsilon_i \Phi_i^{(n)} + \frac{q_j}{\epsilon_0 h}}{\sum_{i=1}^{6} \epsilon_i + \epsilon_{solv} \left(\frac{h}{\lambda}\right)^2} \right) + (1 - \omega) \, \Phi_j^{(n)} \tag{A.4}$$

The best over-relaxation factor can be obtained from the highest eigenvalue of the iteration matrix [42], which in turn can be calculated using the Connected-Moments Expansion [28]. This stencil was first used in [45] and a revision of its uses (at the time or writing) can be found in [40]. Later the stencil has been parallelized using MPI in [22], and using CUDA but with different kernels in [9] and [41].

In order to obtain a well defined solution, suitable boundary conditions must be ensured, the interested reader can find some details on different available alternatives in the work of Rocchia, which focuses on biological applications [33].

A.1.1 Exploiting the structure of the system

The following observations help significantly to improve the efficiency of the algorithm. First, if the number of grid points in the first two dimensions is odd, the discretized FD scheme is endowed with the so called checkerboard structure. All even grid points depend only on their neighboring grid points, which are odd, and *vice versa*. This allows to iterate alternately on grid points of different parity until convergence. Due to this property, one can break the dependence imposed by the formula (A.3) and apply the parallelism inside each of the even/odd steps. Second, it is worth pointing out that on most grid points no charges are mapped and also are located in a uniform dielectric region, where ϵ_i is constant. In most of the cases, indeed, ϵ varies only around the molecular surface. Due to these observations, the stencil can be simplified as follows:

$$\Phi_j = \frac{\sum_{i=1}^{6} \Phi_i}{6 + \kappa_j^2} \tag{A.5}$$

where

$$\kappa_j = \begin{cases} \left(\frac{h}{\lambda}\right) & \text{if } j \text{ is inside the ionic solution,} \\ 0 & \text{otherwise.} \end{cases} \tag{A.6}$$

allowing a faster parallelization. After each run of this uniform stencil, corrections have to be made at the points where charges are present and where ϵ_i changes. This solution is therefore faster than using the full non uniform stencil on the whole grid.

Contiguous memory mapping

Instead of making the numerical computations and moving the memory access along a three dimensional parallelepiped and updating the odd and even points, the solution was calculated using two 1-D pointers: one for the even and one for the odd grid points, Φ_e and Φ_o respectively. Every grid point $p_o(x_o, y_o, z_o)$ is mapped into an odd p_{odd} or even p_{even} pointer according to the rule:

$$\begin{aligned} p_{even} &= \frac{x_o + n_x y_o + n_x n_y z_o}{2} \\ p_{odd} &= \frac{x_o + n_x y_o + n_x n_y z_o - 1}{2} \end{aligned} \tag{A.7}$$

so that the update of each pointer depends only upon the one with opposite parity. The offset of the indexing of the neighboring points in this case can be seen in Table A.1. In Figure A.1 we show a 3D graphical representation of the checkerboard structure and its relationship with the arrays used for the continuous memory mapping.

Table A.1: Neighbor offsets for even and odd points

Neighbor	Offset when p_o is even	Offset when p_o is odd
Left $(-X)$	-1	$+1$
Right $(+X)$	0	0
Back $(-Y)$	$-\frac{(n_x+1)}{2}$	$-\frac{(n_x-1)}{2}$
Front $(+Y)$	$+\frac{(n_x-1)}{2}$	$+\frac{(n_x+1)}{2}$
Bottom $(-Z)$	$-\frac{(n_x n_y+1)}{2}$	$-\frac{(n_x n_y-1)}{2}$
Top $(+Z)$	$+\frac{(n_x n_y-1)}{2}$	$+\frac{(n_x n_y+1)}{2}$

A.1.2 Sequential algorithm

Due to the corrections that have to be made after the uniform stencil is applied, namely on the regions where the dielectric constant is not uniform and where charges are present, a preprocessing stage is needed to identify the pointers corresponding to the grid points located in these regions. These steps are:

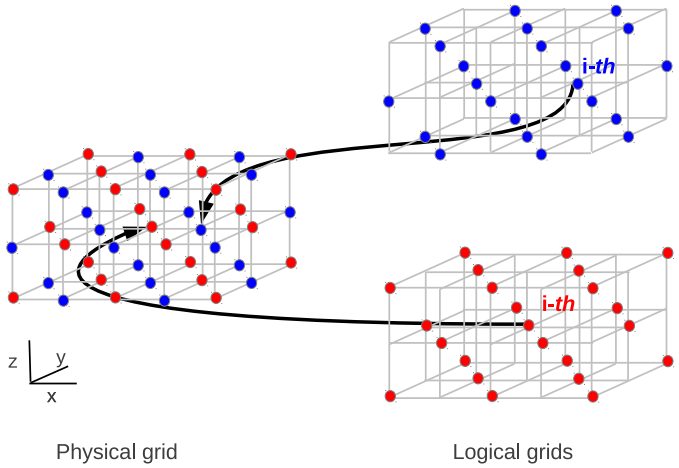

Figure A.1: Checkerboard structure used to build the continuous memory mapping.

- **Determine inside/outside**. Determine which grid points are on the solute or in the solvent, this involves the calculation of the molecular surface of the solute (see [11] for a summary of the different possibilities). If there is salt in the solution we also calculate the κ factor.
- **Find dielectric boundaries and prepare the boundaries correction**. Look for the midpoints in which ϵ_i varies and calculate the correction to be applied after the stencil operation.
- **Set boundary conditions**. Set up the boundary conditions to be used, see [33] for a description of the possibilities.
- **Prepare charges correction**. Calculate the correction to be applied to the grid points where charges have been assigned.

After that, the main iteration then applies the uniform Laplace stencil to the grid points of one parity, and afterward it corrects where needed. Then the opposite parity points are updated, with the corresponding correction. The convergence of the iterative scheme is evaluated using the maximum difference of the potential on the grid every 10 iterations. The steps of the main loop are the following:

1. **Save dielectric boundaries**. Save the state of the dielectric boundary points considering a temporary vector for convergence test at the end.
2. **Run Poisson or Poisson-Boltzmann**. This is the main calculation block that implements the stencil given by Equation (A.5) and is executed on every grid point.
3. **Adjust dielectric boundaries**. Update the potential value of the grid points located at the dielectric boundary, this is done at the end of each iteration.
4. **Add charges**. Add the charge terms to the grid points that were predefined as charged.
5. **Calculate potential difference at the dielectric boundary**. Calculate the absolute differences between the current potential values at the dielectric boundary with the one saved previously on a temporary data structure. This is done since the boundary is the region where the convergence is expected to be slower.
6. **Check convergence**. The maximum absolute difference between the potential at two subsequent iterations is compared to the threshold to test the convergence and to decide whether to stop the iterative procedure.

In the remaining of the paper, for each parallel implementation of the full Poisson-Boltzmann solver, we refer to this list to explain the adopted approach.

A.2 MPI Implementation

The implementation described in this Section was developed to enable the run of the numerical solver on distributed memory architectures such as cluster of (multicore) CPUs. This kind of architectures can be exploited using well-known SPMD (Single Program Multiple Data) programming model on distributed memory resources; the standard de facto in this context is MPI.

The approach adopted considers a data parallelism, i.e. the global data set is subdivided in partial data sets elaborated in parallel. The volume storing input data was subdivided in smaller parallelepipeds; the number of the subdomains relies on the number of MPI processes spawned for the computation, in fact each subdomain is assigned to a MPI parallel process that is in charge of its elaboration. The volume subdivision among the parallel processes was implemented using the parallel I/O functionalities provided by MPI (version 2 and onwards). The exploitation of this feature enabled the speedup of data distribution; in fact we avoided the master-slave approach, i.e. only one process (the master) accesses the data set and distributes data among the other processes (the slaves), that results in a more time consuming phase. Furthermore,

the use of the MPI2 parallel I/O ensures optimized parallel accesses to the data set thus reducing data contention.

In the checkerboard structure used to solve the Laplace equation, there is the need to consider for each point of the grid its 6 neighbors of opposite parity. Therefore, subdomains have to take into account overlapping areas to properly manage this requirement, and MPI data communications were introduced to exchange the neighbor points at the border of each subdomain. This marks a different approach from the one taken at [22], where authors used the direct remote memory access (DRMA) to manage the neighbor points.

The domain was divided along the most external dimension, i.e. Z. Therefore, the dimensions of the subdomain elaborated by the MPI processes are parallelepipeds with the same X and Y dimensions, but with a lower number of layers on Z. For each subdomain, also charges, dielectric boundaries and the value of κ were assigned. Note that the communications involve even and odd grid points, so particular care is devoted to enforce the consistency of the parity of the points. In fact, since each subdomain acts as an independent solver, all subdomains assume that the first grid point is even. This has to be ensured during the subdivision of the domain. This problem was solved by dividing the domain so as that each subdomain starts with an even grid point, and a consequent management in the whole data set.

Defining N_z as the total number of levels/layers on the Z axis of the whole domain, $nproc$ the number of MPI processes spawn, and i the process identifier, the algorithm employed to calculate the number of layers n_z^i on the subdomain i is described in Algorithm 1.

Algorithm 1 Algorithm for the division of the computation domain.

for all $i \in [0, nproc-1]$ **do**
  $n_z^i = floor(N_z/nprocs)$
  if $modulo(n_z^i, 2) \neq 0$ **then**
    $n_z^i = n_z^i - 1$
  end if
  $res1 = N_z - n_z^i \cdot nproc$
  $nres = res1/2$
  $res2 = module(res1, 2)$
  if $i = 0$ **then**
    $n_z^i = n_z^i - 1$
    if $nres > 0$ **then**
      $n_z^i = n_z^i + 2$
    end if
  else if $i = nproc - 1$ **then**
    $n_z^i = n_z^i + 1$
    if $res2! = 0$ **then**
      $n_z^i += res2$
    end if
  else if $i < nres$ **then**
    $n_z^i = n_z^i + 2$
  end if
end for

To understand how the algorithm works note that many conditions have to be imposed for the parity consistency and to properly manage the boundary requirements, e.g. the first and the last Z levels on the whole volume have only one border to consider, while the other levels have to allocate two borders, one layer above and one below.

Once each subdomain is constructed, the solver acts in each subdomain almost as the sequential version would, and only minor modifications are needed. The boundary conditions on the faces perpendicular to the X and Y axes are calculated as in the sequential case, and the boundary on faces perpendicular to Z requires the values that have to be exchanged exploiting MPI except for the first and last subdomains, where one of the faces actually corresponds to a boundary. A border is composed of 2 layers (one for each overlapping subdomain), thus for each iteration 4 layers have to be sent and 4 received. This is done after the update of the potential for each parity. Since the data transferred is needed right after the data communication occurs, only *blocking communications* were used.

A.3 MPI vs OpenMP implementations

In the case of one multicore node, i.e. shared memory cores, it is interesting to compare the performance achievable using two different parallel libraries to exploit a shared memory architecture, as MPI and OpenMP. For this reason, we develop an OpenMP implementation of the solver.

The parallelization on multicore nodes using OpenMP is the easiest approach to implement. Pragma clauses were added at FD stencil, as it is by far the more computationally expensive part of the code. This can be considered equivalent to sub-dividing the volume containing the input dataset in cuboids, as done in the MPI parallelization and described in A.2. Static scheduling was used, setting the chunk of each thread manually so that they are evenly distributed.

As in the CUDA, we combined this implementation with the one developed using MPI thus to exploit cluster of multicore CPUs; again, the effort spent to integrate the codes was actually affordable. The algorithm implements the MPI subdomain definition, thus distributing data among MPI parallel processes; on each data set the OpenMP code is executed, while the MPI process manages data communications among the non-shared memory nodes. In that way, MPI controls the communication between nodes and OpenMP the parallelization in each node.

A.4 Experimental Results

We had the possibility to test the implementations described in this paper on several parallel resources corresponding to different architectures. The configuration of each resource can be seen on Table A.2. All tests used the same molecule with the same parameters: a Fatty Acid Amide Hydrolase molecule that, once ported to the cubic grid, consisted of 29880 charges on $297x297x297$ grid points. A salt concentration of $0.15mol/l$ and dipolar boundary conditions were used. In the following Subsections we discuss the different results obtained by adopting the implementations previously presented.

Table A.2: Resources used for testing

Resource	Nodes	Cores per node	Network	Chip
Cluster 1	8	8	Infiniband	Quad-Core AMD Opteron Processor 2352
Cluster 2	2	12	1G ethernet	Intel Xeon E5645

A.4.1 MPI performance

In Figures A.2 and A.3 we present the results of Section A.2 obtained on Cluster 1 and Cluster 2 respectively. Both refer to the linear PBE. In order to appreciate the impact of the different parts of the algorithm we differentiate among the whole execution time, depicted with a blue line, the time required for data distribution and communication, indicated as MPI and depicted with a red line, and the time used on the stencil indicated as Bolzmann and depicted with a brown line. The calculation of the Boltzmann stencil was the most demanding one in terms of execution time, the time spent on communications instead depends on the resource. In fact, it is possible to notice that on Cluster 2, the absence of InfiniBand was heavily affecting computation since more time was spent in data transfer than iterating at the Boltzmann stencil, by far the most computationally expensive part of the algorithm. To make a fair comparison of the results obtained on the different resources, the time spent in MPI communications was not more reported.

In Figure A.4, we present the execution time of a single iteration of the linear Boltzmann stencil on Clusters 1 and 2. It was obtained an impressive decrease of the execution time. However the speed up values are not linear. This is to be expected since the problem we are solving is a data intensive problem.

A.4.2 MPI and OpenMP performance

It is interesting to compare the results obtained using the MPI and OpenMP implementations on the same shared memory node, which can be seen on Figure A.6. To test the MPI and OpenMP implementation, we used the three nodes of Cluster 2, spawning three MPI processes and 12 OpenMP thread. Results are depicted in Figure A.7. The number of cores was increased equally on all nodes. Neither of the implementations achieved good results. Since the stencil involves a lot of memory access, in a shared memory environment this could slow down the performance. On the other hand, we have to stress the easiness of the parallelization with OpenMP, definitively much more significant than MPI. The MPI performance payed the effort spent to develop that implementation.

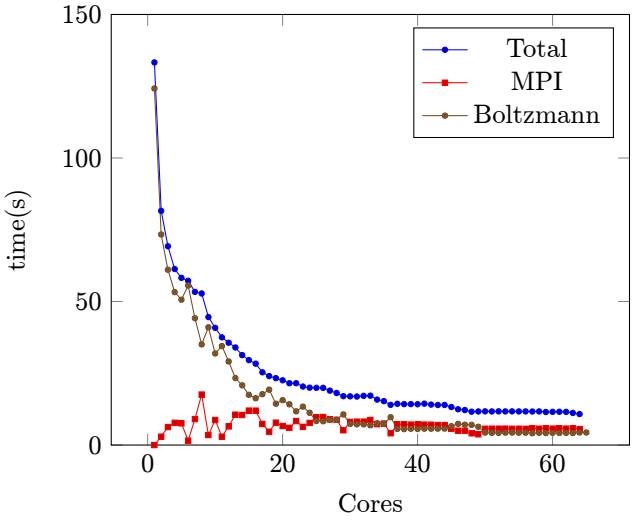

Figure A.2: MPI results on Cluster 1. The whole execution time is depicted with a blue line, the time required for data communication is indicated as MPI and depicted with a red line, the stencil part of the solver is indicated as Bolzmann and depicted with a black line.

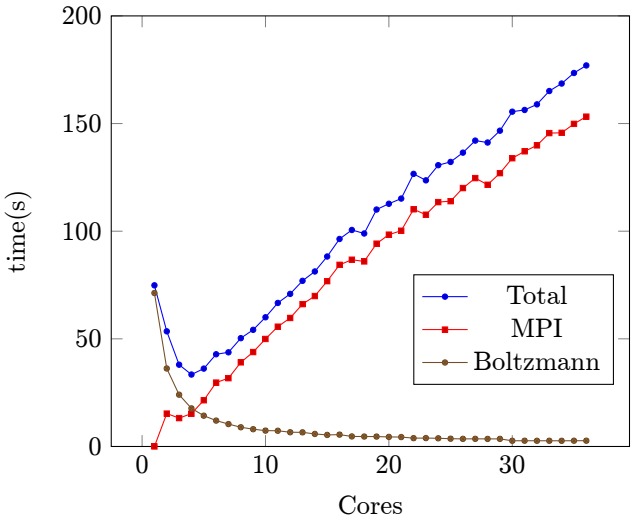

Figure A.3: MPI results on Cluster 2. The whole execution time is depicted with a blue line, the time required for data communication is indicated as MPI and depicted with a red line, the stencil part of the solver is indicated as Bolzmann and depicted with a black line. When this Figure is compared with Figure A.2, InfiniBand proved to be crucial. Its absence meant that more time was spent on data communication rather than doing calculations.

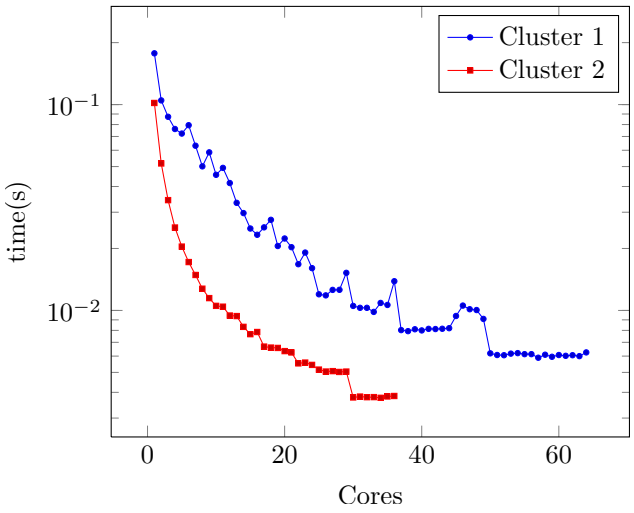

Figure A.4: Execution time per iteration of the linear Boltzmann stencil versus number of cores done on Clusters 1 and 2.

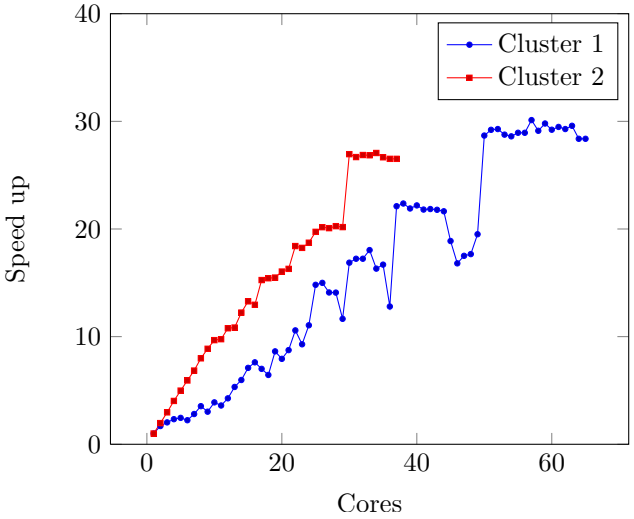

Figure A.5: Speed up of the execution time per iteration of the linear Boltzmann stencil versus number of cores done on clusters 1 and 2.

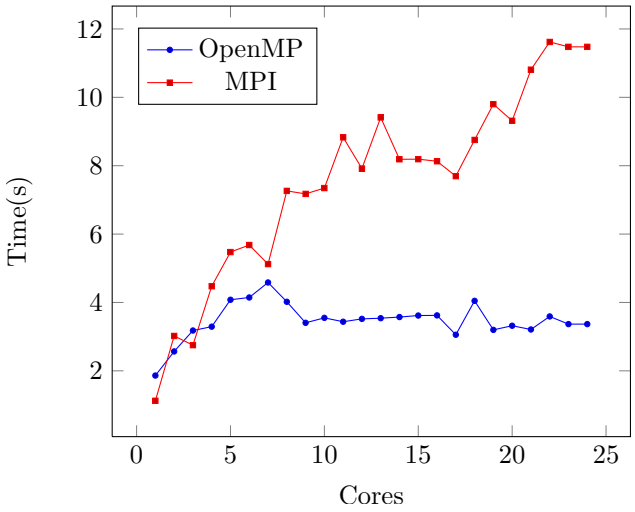

Figure A.6: Comparaison of the speedup on the stencil between MPI and OpenMP on Cluster 3.

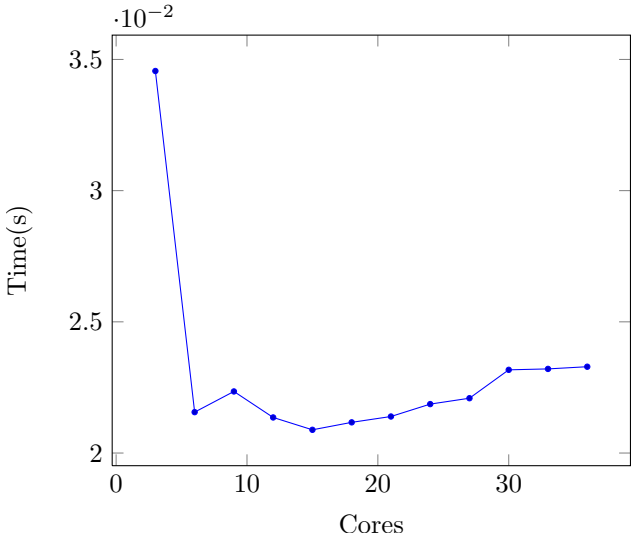

Figure A.7: Execution time per iteration of the linear Boltzmann stencil versus number of cores used through OpenMP and MPI working toguether on Cluster 2.

Bibliography

[1] Binley A., Slater L., Fukes M., and Cassiani G. The relationship between spectral induced polarization and hydraulic properties of saturated and unsaturated sandstone. *Water Resources Research*, 41(12), 2005.

[2] Bucker A. and Hordt A. Long and short narrow pore models for membrane polarization. *Geophysics*, 78, 2013.

[3] Kemna A. *Tomographic inversion of complex resistivity: Theory and applications.* PhD thesis, Ruhr-University of Bochum., 2000.

[4] Revil A. and Florsch N. Determination of permeability from spectral induced polarization data in granular media. *Geophysical Journal International*, 181:1480–1498, 2010.

[5] A. Angulo-Sherman and H. Mercado-Uribe. Dielectric spectroscopy of water at low frequencies: The existence of an isopermitive point. *Chemical Physics Letters*, 503:327–330, 2011.

[6] T.M.W.J. Bandara and B.-E. Mellander. *Evaluation of Mobility, Diffusion Coefficient and Density of Charge Carriers in Ionic Liquids and Novel Electrolytes Based on a New Model for Dielectric Response, Ionic Liquids: Theory, Properties, New Approaches.* Intech, 2011.

[7] John O'M Bockris and Amulya KN Reddy. *Modern Electrochemistry 2B: Electrodics in Chemistry, Engineering, Biology and Environmental Science*, volume 2. Springer, 2000.

[8] Y. Chen and D. Or. Effects of maxwell-wagner polarization on soil complex dielectric permittivity under variable temperature and electrical conductivity. *Water Resour. Res.*, 42, 2006.

[9] J. Colmenares, J. Ortiz, S. Decherchi, A. Fijany, and W. Rocchia. Solving the linearized poisson-boltzmann equation on gpus using cuda. In *21st Euromicro International Conference on Parallel, Distributed, and Network-Based processing.* IEEE Computer Society, 2013.

[10] P. Debye and E. Huckel. Zur theorie der elektrolyte. *Physik. Zeits.*, 24, 1923.

[11] Sergio Decherchi, Jose Colmenares, Chiara E. Catalano, Michela Spagnuolo, Emil Alexov, and Walter Rocchia. Between algorithm and model:

different molecular surface definitions for the poisson-boltzmann based electrostatic characterization of biomolecules in solution. *Commun. Comput. Phys.*, 13:61–89, 2012.

[12] Marshall D.J and Madden T. K. Induced polarization, a study of its causes. *Geophysics*, 24:790–816, 1958.

[13] DA Fridrikhsberg and MP. Sidorova. Issledovanie sviazi yavlenia vyzvannoi polarizatsii s electrokineticheskimi svoistvami kapillamyh sistem (a study of relationship between the induced polarization phenomenon and the electrokinetic properties of capillary systems). *Vestnik Leningradskogo Universiteta. Seria Chimia*, 4:222 – 226, 1961.

[14] Cassiani G., Kemna A., Villa A., and Zimmermann E. Spectral induced polarization for the characterization of free-phase hydrocarbon contamination of sediments with low clay content. *Near Surface Geophysics*, 7:547–562, 2009.

[15] C Gabriel, S Gabriel, and E Corthout. The dielectric properties of biological tissues: I. literature survey. *Phys. Med. Biol.*, 41:2231–2249, 1996.

[16] Pawel Grochowski and Joanna Trylska. Continuum molecular electrostatics, salt effects, and counterion binding–review of the poisson-boltzmann theory and its modifications. *Biopolymers*, 89:93–113, 2007.

[17] B. Honig and A. Nicholls. Classical electrostatics in biology and chemistry. *Science*, 268:1144–1149, 1995.

[18] Volkmann J. and Klitzsch N. Frequency-dependent electric properties of microscale rock models for frequencies from one millihertz to ten kilohertz. *Vadose Zone J.*, 9:858–870, 2010.

[19] Scott J.B.T. and Barker R.D. Determining pore-throat size in permotriassic sandstones from low-frequency electrical spectroscopy. *Geophys. Res. Lett.*, 30, 2003.

[20] D. Jougnot, A. Ghorbani, A. Revil, and P. Leroy. Spectral induced polarization of partially saturated clay-rocks: a mechanistic approach. *Geophys. J. Int.*, 180:210–224, 2010.

[21] Maria G. Kurnikova, Rob D. Coalson, Peter Graf, , and Abraham Nitzan. A lattice relaxation algorithm for three-dimensional poisson-nernst-planck theory with application to ion transport through the gramicidin a channel. *Biophysical Journal*, 76:642–656, 1999.

[22] Chuan Li, Lin Li, Jie Zhang, and Emil Alexov. Highly efficient and exact method for parallelization of grid-based algorithms and its implementation in delphi. *Journal of Computational Chemistry*, 2012.

[23] De Lima, OAL, and MM Sharma. A generalized maxwell-wagner theory for membrane polarization in shaly sands. *Geophysics*, 57, 1992.

[24] Ali Mani, Thomas A. Zangle, and Juan G. Santiago. On the propagation of concentration polarization from microchannel-nanochannel interfaces part i: Analytical model and characteristic analysis. *Langmuir*, 25:3898–3908., 2009.

[25] DJ. Marshall and TR. Madden. 1959 induced polarization, a study of its causes. *Geophysics*, 24.:790–816., 1959.

[26] SS. Mohamed. Induced polarization, a method to study water-collecting properties of rocks. *Geophysical Prospecting*, 18, 1970.

[27] Hiromu Monai, Masashi Inoue, Hiroyoshi Miyakawa, and Toru Aonishi. Low-frequency dielectric dispersion of brain tissue due to electrically long neurites. *Phys. Rev. E*, 86:061911, Dec 2012.

[28] A. Nicholls and B. Honig. A rapid finite difference algorithm, utilizing successive over-relaxation to solve the poisson-boltzmann equation. *Journal of Computational Chemistry*, 12:435–445, 1991.

[29] Leroy P. and Revil A. A mechanistic model for the spectral induced polarization of clay materials. *J. geophys. Res. B: Solid Earth.*, 114, 2009.

[30] Leroy P. and Revil A. Spectral induced polarization of clays and clay-rocks. *J. geophys. Res.*, 114., 2009.

[31] Leroy P., Revil A., Kemna A., and Cosenza P. Complex conductivity of water-saturated packs of glass beads. *Journal of Colloid and Interface Science*, 321:103–117., 2008.

[32] Zheng Ql., Chen D., and Wei GW. Second-order poisson nernst-planck solver for ion channel transport. *J Comput Phys.*, 230:5239–5262., 2011.

[33] Walter Rocchia. Poisson-boltzmann equation boundary conditions for biological applications. *Mathematical and Computer Modelling*, pages 1109–1118, 2005.

[34] Walter Rocchia, Emil Alexov, and Barry Honig. Extending the applicability of the nonlinear poisson-boltzmann equation: Multiple dielectric constants and multivalent ions. *J. Phys. Chem. B*, 105:6507–6514, 2001.

[35] Walter Rocchia, Sridhar Sridharan, Anthony Nicholls, Emil Alexov, Alessandro Chiabrera, and Barry Honig. Rapid grid-based construction of the molecular surface for both molecules and geometric objects: Applications to the finite difference poisson-boltzmann method. *Journal of Computational Chemistry*, 23:128–137, 2002.

[36] Lech Rusiniak. Electric properties of water. new experimental data in the 5 hz – 13 mhz frequency range. *ACTA GEOPHYSICA POLONICA*, 52(1), 2004.

[37] Kruschwitz S., Binley A., Lesmes D., and Elshenawy A. Physical controls on low frequency electrical spectra of porous media. *Geophysics*, 75:WA113–WA123., 2010.

[38] JM. Schurr. On the theory of the dielectric dispersion of spherical colloidal particles in electrolyte solution. *Journal of Physical Chemistry*, 68:2407–2413., 1964.

[39] G. Schwarz. A theory of the low-frequency dielectric dispersion of colloidal particles in electrolyte solution. *Journal of Physical Chemistry*, 66:2636–2642, 1962.

[40] K. Sharp and B. Honig. Electrostatic interactions in macromolecules: Theory and applications. *Ann. Rev. Biophys. Biopys. Chem.*, 19:301–32, 1990.

[41] Nikolay A. Simakov and Maria G. Kurnikova. Graphical processing unit accelerated poisson equation solver and its application for calculation of single ion potential in ion-channels. *Molecular Based Mathematical Biology*, 1:151–163, 2013.

[42] J. Stoer and R. Bulirsch. *Numerical Mathematics*. Springer, 2002.

[43] K. Titov, V. Komarov, V. Tarasov, and A. Levitski. Theoretical and experimental study of time domain induced polarization in water-saturated sands. *Journal of Applied Geophysics*, 50:417–433, 2002.

[44] HJ. Vinegar and MH. Waxman. Induced polarization of shaly sands. *Geophysics.*, 49:1267–1287., 1984.

[45] J. Warwicker and H.C. Watson. Calculation of the electric potential in the active site cleft due to alpha-helix dipoles. *Journal of Molecular Biology*, 157(4):671 – 679, 1982.